

## Article

# A Numerical Study on the Response of a Very Large Floating Airport to Airplane Movement

Taro Kakinuma <sup>1,\*</sup>  and Masaki Hisada <sup>2</sup><sup>1</sup> Graduate School of Science and Engineering, Kagoshima University, Kagoshima 890-0065, Japan<sup>2</sup> Faculty of Engineering, Kagoshima University, Kagoshima 890-0065, Japan

\* Correspondence: taro@oce.kagoshima-u.ac.jp; Tel.: +81-99-285-8467

**Abstract:** Numerical simulations were generated to investigate the response of a floating airport to airplane movement using the nonlinear shallow water equations of velocity potential for water waves interacting with a floating thin plate. First, in the 1D calculations, the airplanes were B747 and B737. At touch-and-go, when the airplane speed is closer to the water wave speed, even B737 produced large waves based on the resonance. The impacts due to both the touchdown and leaving of the airplanes generated other forward and backward waves. At landing, when the airplane speed approached the water wave speed, a forced wave was generated and amplified, with many free waves ahead. At takeoff, a wave clump, generated shortly after starting to run, propagated in front of the airplanes. Although the wave height increased from superposition with the reflected waves, the wave reflectance was reduced by lowering the flexural rigidity near the airport edge. Second, in the 2D calculations, B787 performed landing and takeoff. When the still water depth is shallower, a grid-like pattern was formed at the floating airport and appeared more remarkably in landing than in takeoff. The effective amplification occurred from a sufficient load applied when the airplane speed approached the water wave speed. Furthermore, the maximum upslope gradient beneath the airplane increased as the still water depth decreased, and it was larger in takeoff than in landing.

**Keywords:** very large floating structure; VLFS; offshore airport; landing; takeoff; touch-and-go; hydroelasticity; resonance; wave reflection



**Citation:** Kakinuma, T.; Hisada, M. A Numerical Study on the Response of a Very Large Floating Airport to Airplane Movement. *Eng* **2023**, *4*, 1236–1264. <https://doi.org/10.3390/eng4020073>

Academic Editor: Antonio Gil Bravo

Received: 12 February 2023

Revised: 11 April 2023

Accepted: 14 April 2023

Published: 21 April 2023



**Copyright:** © 2023 by the authors. Licensee MDPI, Basel, Switzerland. This article is an open access article distributed under the terms and conditions of the Creative Commons Attribution (CC BY) license (<https://creativecommons.org/licenses/by/4.0/>).

## 1. Introduction

A very large floating structure, a VLFS, which is designed to be an offshore airport, storage facility, wind/solar power plant, evacuation area in disaster events, or others, has advantages such as towability and environmental friendliness due to the ability of seawater to flow under the structure. In recent years, techniques to obtain sustainable energy by converting water wave energy using floating flexible structures have also been devised, e.g., [1,2]. Such floating structures exist at sea, i.e., on a fluid, and because of their large size, they deform and vibrate based on hydroelasticity. Therefore, to design a VLFS, it is necessary to understand the interaction between the oscillation of the structure and the motion of the fluid. For the design of a flexible VLFS interacting with wind waves including typhoon-driven waves, various models have been developed, e.g., [3–9].

Even in nature, the interaction between flexible platforms and a fluid can be observed when ice plates float on the sea surface [10]. The effects of floating ice in different forms on water waves have been studied [11–14], and the response of an ice plate to a moving load on it has also been investigated [15–17]. These results can be referred to when designing a VLFS.

Regarding the response of a VLFS to long waves including tsunamis, the Boussinesq-type equations for surface waves were solved numerically using a finite difference method (FDM) to examine the relationship between the bending moment and flexural rigidity of a floating thin plate on a progressing solitary wave [18]. The interaction of a thin plate with

an incident solitary wave was also investigated by coupling a finite element method (FEM) and boundary element method (BEM) in two vertical dimensions [19]. This interaction was also reproduced by hydraulic experiments, and the solitary waves were disintegrated by the floating thin plate, as their nonlinearity was strong [19]. The results—the wave height of the incident waves decreased because of the generation of floating-body waves—suggest that the wave height of a huge tsunami decreases after propagating through an offshore VLFS. The tsunami-height reduction using a VLFS was discussed based on the numerical simulation of water waves interacting with a floating thin plate using an FDM [20].

When density stratification is developed under a floating structure, its oscillation may generate internal waves, leading to a change in seawater salinity and temperature, especially in coastal environments, through the propagation, shoaling, and breaking of the internal waves. To study the response of a floating thin plate in a coexisting field of surface and internal waves, a vertical two-dimensional problem was formulated with the framework of a linear potential theory [21]. The surface/internal waves due to a moving load on a VLFS in two vertical dimensions were examined using an FDM, considering both the nonlinearity and dispersion of the water waves [22].

One of the artificial loads on a VLFS is the movement of airplanes on a floating airport, and cases of an airplane moving on a floating airport have also been studied. For example, the drag against an airplane taking off from a floating airport of infinite length was evaluated numerically, using the Fourier transform theory, for different flexural rigidities of the airport [23]. Conversely, the transient response of a floating airport under the load of a landing airplane was studied using an FEM [24]. In the coexistence field of linear waves and a current, a BEM was applied to simulate the thin plate response to a moving weight [25]. Under the combined loads of water waves and an airplane landing or taking off, the time variation of an airport profile and the drag induced on an airplane by the deformed runway were obtained using both an FEM-scheme-based method and Wilson's  $\theta$  method [26]. The horizontally two-dimensional linear response of a floating airport to the landing and takeoff of an airplane was investigated using the time-domain mode expansion method [27]. Moreover, a combination of a BEM and moving element method (MEM) was utilized to study the hydroelastic response of floating composite plates subjected to moving loads [28].

In the present paper, an offshore airport is assumed as a floating thin plate, and its oscillation due to airplane movement—touch-and-go, landing, and takeoff—is discussed based on numerical simulations with an FDM. The governing equations were the nonlinear shallow water equations on velocity potential, which were obtained by reducing the equations obtained based on a variational principle for water waves, considering the flexibility of floating thin plates [29]. In the numerical calculations, the flexural rigidity is given at the location of a thin plate to express the thin plate covering part of the water area. With this method, it is possible to consider the reflection and transmission of waves at the edges of the thin plate, so we also discuss the reflection and transmission of floating-body waves, which were not discussed for infinite length airports. First, we investigate the response of a very large floating airport to the movement of two sizes of jetliners in one-dimensional problems. Thereafter, we discuss horizontally two-dimensional problems of the behavior of the floating airport due to the movement of a medium-sized jetliner.

## 2. Numerical Calculation Method

### 2.1. Governing Equations

The illustration in Figure 1 is our schematic for a system consisting of multilayer fluids and thin plates, where the fluid layers and thin plates are represented as the  $i$ -layers and  $i$ -plates ( $i = 1, 2, \dots, I$ ) from top to bottom, respectively.

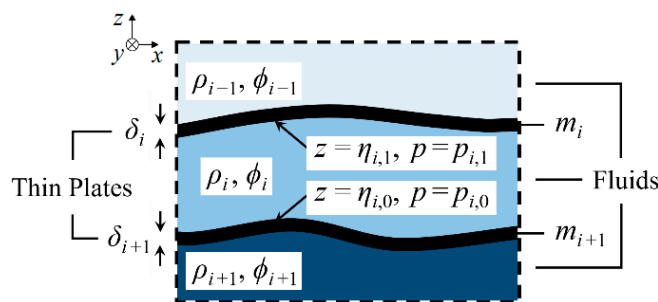


**Figure 1.** Schematic for a system consisting of multilayer fluids and thin plates.

We assume that none of the fluids mix even in motion without plates, and the density  $\rho_i$  ( $\rho_1 < \rho_2 < \dots < \rho_l$ ) of the  $i$ -layer is spatially uniform and temporally constant in each layer. The thickness of the  $i$ -layer is  $h_i(x)$  in still water, where  $x$  is the coordinate in the horizontal plane, namely  $(x, y)$ . The origin of the vertical axis  $z$  is located at the top surface of the system in the stationary state, and the positive direction of  $z$  is vertically upward. The elevations of the lower and upper interfaces of the  $i$ -layer are expressed by  $z = \eta_{i,0}(x, t)$  and  $z = \eta_{i,1}(x, t)$ , respectively, and the pressures at the lower and upper interfaces of the  $i$ -layer are defined as  $p_{i,0}(x, t)$  and  $p_{i,1}(x, t)$ , respectively.

The thin plate touching the upper interface of the  $i$ -layer is called the  $i$ -plate. The density and vertical width of the  $i$ -plate are  $m_i$  and  $\delta_i$ , respectively. When  $m_i$ ,  $\delta_i$ , and the flexural rigidity of the  $i$ -plate are zero, the plate yields no resistance to fluid motion, where two immiscible fluids touch each other directly without any plate. Both surface tension and capillary action are ignored, and friction is also ignored for simplicity. Moreover, the energy attenuation inside the thin plates is not considered.

We assume that the fluids are inviscid and incompressible, and fluid motion is irrotational, resulting in the existence of velocity potential  $\phi_i$  in the  $i$ -layer, and  $\phi_i$  is expanded into a power series of  $z$  with weightings  $f_{i,\alpha}$  as

$$\phi_i(x, z, t) = \sum_{\alpha=0}^{N_i-1} [f_{i,\alpha}(x, t) \cdot z^\alpha], \tag{1}$$

where  $N_i$  is the number of terms for an expanded velocity potential in the  $i$ -layer.

In the  $i$ -layer, when both the displacement of one interface,  $z = \eta_{i,1-j}(x, t)$  ( $j = 0$  or  $1$ ), and the pressure on the other interface,  $p_{i,j}(x, t)$ , are known, the unknown variables are the velocity potential  $\phi_i(x, z, t)$  and interface displacement  $\eta_{i,j}(x, t)$ . Then, the definition of the functional for the variational problem in the  $i$ -layer,  $F_i$ , is as follows [29]:

$$F_i[\phi_i, \eta_{i,j}] = \int_{t_0}^{t_1} \iint_A \int_{\eta_{i,0}}^{\eta_{i,1}} \left[ \frac{\partial \phi_i}{\partial t} + \frac{1}{2}(\nabla \phi_i)^2 + \frac{1}{2} \left( \frac{\partial \phi_i}{\partial z} \right)^2 + gz + \frac{p_{i,j} + P_i + W_i}{\rho_i} \right] dz dA dt, \tag{2}$$

where  $\nabla = (\partial/\partial x, \partial/\partial y)$  is a horizontal partial differential operator, and the gravitational acceleration  $g$  is  $9.8 \text{ m/s}^2$ . The plane  $A$ , which is the orthogonal projection of the object domain on to the  $x$ - $y$  plane, is assumed to be independent of time.

In comparison with the functional referred to in [30] for the rotational motion of a fluid, Equation (2) introduces an additional term of the integral of  $(p_{i,j} + P_i + W_i)/\rho_i$  as an interfacial pressure term, without the terms related to vorticity. Using the functional of [30], after omitting the vorticity terms, the set of nonlinear equations for one-layer problems without thin plates was derived by [31].

$P_i$  and  $W_i$  in Equation (2) are expressed by

$$P_i = \sum_{k=1}^{i-1} [(\rho_i - \rho_k)gh_k], \tag{3}$$

$$W_i = \sum_{k=1}^i (-m_k g \delta_k), \tag{4}$$

respectively, in the case of no buoyancy of the structures.

After substituting the velocity potential  $\phi_i$  expanded in Equation (1) into Equation (2), the Euler–Lagrange equations on  $\eta_{i,j}$  and  $f_{i,\alpha}$  are derived as

$$\eta_{i,1}^\alpha \frac{\partial \eta_{i,1}}{\partial t} - \eta_{i,0}^\alpha \frac{\partial \eta_{i,0}}{\partial t} + \nabla \left[ \left( \eta_{i,1}^{\alpha+\beta+1} - \eta_{i,0}^{\alpha+\beta+1} \right) \nabla f_{i,\beta} \right] - \frac{\alpha\beta}{\alpha + \beta - 1} \left( \eta_{i,1}^{\alpha+\beta-1} - \eta_{i,0}^{\alpha+\beta-1} \right) f_{i,\beta} = 0, \tag{5}$$

$$\eta_{i,j}^\beta \frac{\partial f_{i,\beta}}{\partial t} + \frac{1}{2} \eta_{i,j}^{\beta+\gamma} \nabla f_{i,\beta} \nabla f_{i,\gamma} + \frac{1}{2} \beta \gamma \eta_{i,j}^{\beta+\gamma-2} f_{i,\beta} f_{i,\gamma} + g \eta_{i,j} + \frac{p_{i,j} + P_i + W_i}{\rho_i} = 0 \quad (j = 0 \text{ or } 1), \tag{6}$$

where the sum rule of product is adopted for subscripts  $\beta$  and  $\gamma$ . For example,  $f_{2,3}$  is the weighting of  $z^3$  in the 2-layer.

For long surface waves in one-layer problems without thin plates, the accuracy of the above equations was investigated by [32]: when the maximum order of equations is  $2n$ , the order of error in the set of Equations (5) and (6) is  $\sigma^{4n+2}$ , where  $\sigma$  is the representative ratio of water depth to wavelength. Conversely, the order of error in the extended Green–Naghdi equation [33] is  $\sigma^{2n+2}$ . Therefore, especially when  $O(\sigma) \ll 1$ , the accuracy of the former is significantly higher than that of the latter for  $n \geq 1$ .

Regarding the  $i$ -plate, the horizontal length scale is assumed to be much larger than the thickness of the thin plate, so the differences in curvature between the upper surface, neutral plane, and lower surface of the thin plate are ignored. Therefore, the governing equation of motion for the  $i$ -plate is the following classical equation to describe the oscillation of an elastic thin plate as

$$m_i \delta_i \frac{\partial^2 \eta_{i,1}}{\partial t^2} + B_i \nabla^2 \nabla^2 \eta_{i,1} + m_i g \delta_i + p_{i-1,0} - p_{i,1} = 0, \tag{7}$$

where  $B_i$  is the flexural rigidity of the  $i$ -plate between the  $(i - 1)$ - and  $i$ -layers. Although both the plate density  $m_i$  and vertical width  $\delta_i$  are assumed to be constant throughout the  $i$ -plate for simplicity, the flexural rigidity  $B_i$  can be distributed along the thin plate.

When the representative values of wave height, wavelength, fluid depth, and density are  $H, l, d$ , and  $\rho$ , respectively, the dimensionless quantities are

$$\left. \begin{aligned} x^* &= \frac{x}{l}, & y^* &= \frac{y}{l}, & t^* &= \frac{\sqrt{gd}}{l} t, & \nabla^* &= l \nabla, & \frac{\partial}{\partial t^*} &= \left( \frac{\partial}{\partial t} \right)^* = \frac{l}{\sqrt{gd}} \frac{\partial}{\partial t}, \\ \eta_{i,e}^* &= \frac{\eta_{i,e}}{H}, & \delta_i^* &= \frac{\delta_i}{H}, & m_i^* &= \frac{m_i}{\rho}, & B_i^* &= \frac{B_i}{\rho g l^4}, & p_{i,e}^* &= \frac{p_{i,e}}{\rho g d} \end{aligned} \right\}, \tag{8}$$

where  $e = 0$  and  $1$ .

We substitute Equation (8) into Equation (7) and obtain

$$\varepsilon^2 \sigma^2 m_i^* \delta_i^* \frac{\partial^2 \eta_{i,1}^*}{\partial t^{*2}} + \varepsilon B_i^* \nabla^{*2} \nabla^{*2} \eta_{i,1}^* + \varepsilon m_i^* \delta_i^* + p_{i-1,0}^* - p_{i,1}^* = 0, \tag{9}$$

where  $\varepsilon = H/d$  and  $\sigma = d/l$  are the representative ratio of wave height to water depth and that of water depth to wavelength, respectively. In a manner similar to that of [18], each layer is assumed to be relatively shallow, so the orders of the parameters are  $O(\varepsilon) = O(\sigma^2) \ll 1$ . Thus, the first term on the left-hand side of Equation (9) can be ignored. Without this term, we obtain the  $i$ -plate equation for the dimensional quantities as

$$B_i \nabla^2 \nabla^2 \eta_{i,1} + m_i g \delta_i + p_{i-1,0} - p_{i,1} = 0. \tag{10}$$

In the present paper, the interaction between surface water waves and a flexible platform floating at the sea surface is discussed, so the velocity potential for the one layer is described as  $\phi(x, z, t) = f_\alpha z^\alpha$ . Thus, the unknown values are the weighting factors  $f_\alpha$  and the surface displacement  $\eta_{1,1}(x, t)$ , which is simply described as  $\zeta(x, t)$  for the horizontally two-dimensional cases and  $\eta(x, t)$  for the one-dimensional cases.

2.2. Numerical Method

The governing equations—Equations (5), (6), and (10)—were transformed to finite difference equations and solved to study the interaction of surface water waves with a floating thin plate. An implicit scheme to solve the present equations without thin plates was developed by [34], in which the two-layer problems between two fixed horizontal plates were solved to simulate one-dimensional propagations of internal waves. We applied this scheme to the equations with a thin plate floating at the sea surface to simulate the propagations of surface waves. This model has been applied for several numerical simulations [20,22,35].

In the initial state at  $t = 0$  s, the weighting coefficients  $f_{i,\alpha}(x, 0)$  of the expanded velocity potential in Equation (1) were all zero, so the initial velocity was zero everywhere. In this paper, the values are written without considering significant digits, although the calculations were conducted using 64-bit floating-point numbers. In the present study, the number of terms for the velocity potential expanded as in Equation (1), i.e.,  $N_1 = N$  was one, so the governing equations were reduced to nonlinear shallow water equations for velocity potential considering the flexural rigidity of a floating thin plate. The numerical calculation method described above is also applicable in this case.

In order to verify the accuracy of this numerical model, the reproducibility of the response of a floating thin plate is examined by comparing the results of numerical computation and those of existing hydraulic experiments. A floating thin plate with a flexural rigidity of  $450 \text{ N}\cdot\text{m}^2$  was installed in a wave channel [19], as sketched in Figure 2.

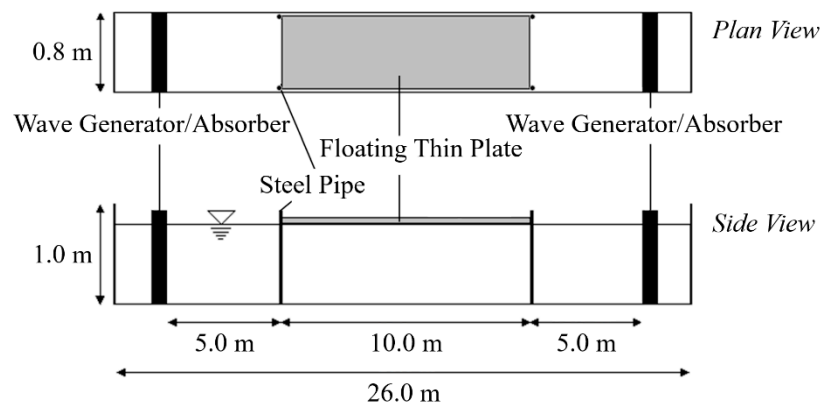


Figure 2. Wave flume used in the hydraulic experiments [19].

In the numerical computation, the computational domain is illustrated in Figure 3. It should be noted that discretization in the  $z$ -axis direction is not performed because the governing equations are vertically integrated equations.

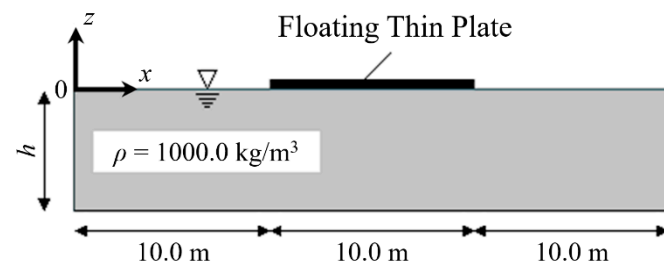
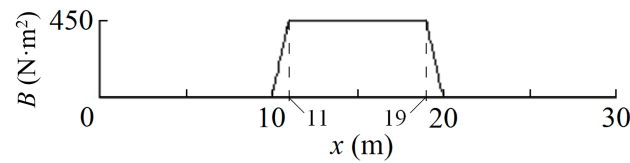


Figure 3. Side view of the computational domain with a floating thin plate.

As depicted in Figure 4, the distribution of the flexural rigidity  $B$  was given at the location of the structure floating at the water surface to express the thin plate covering part of the water area.



**Figure 4.** Distribution of the flexural rigidity at the surface of the computational domain depicted in Figure 3.

The grid sizes and time interval were  $\Delta x = \Delta y = 5.0 \times 10^{-2}$  m and  $\Delta t = 2.5 \times 10^{-5}$  s, respectively. When a solitary wave is incident, Figure 5 presents the experimental and numerical displacements  $\zeta$  of the floating thin plate or water surface at  $x = 7.0$  m and 14.5 m. Based on the results, it is confirmed that the surface displacements in the almost one-dimensional wave propagation were simulated successfully.

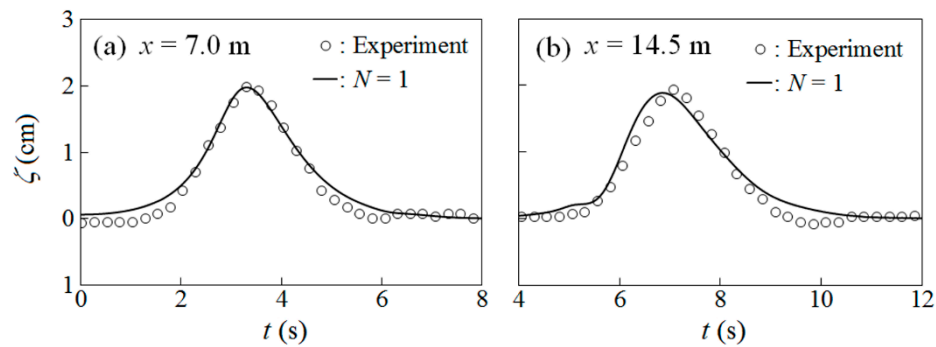


**Figure 5.** Surface displacements  $\zeta$  at  $x = 7.0$  m (a) and 14.5 m (b). The still water depth was 0.4 m and the incident wave height was 0.02 m.

In the present study, we generated numerical calculations for one- and two-dimensional propagations of surface waves. In the 1D calculations, we obtained surface waves generated by two sizes of airplanes with different weights at touch-and-go, takeoff, and landing. When the hydroelastic runway is not so wide compared to the spacing of the aircraft’s left and right landing gears, 1D wave propagation can be dominant. Conversely, in the 2D calculations, we obtained surface wave patterns for different water depths when a medium-sized airplane lands at or takes off from a floating airport.

### 3. Calculation Conditions

#### 3.1. 1D Calculations

##### 3.1.1. Common Conditions

In the 1D calculations, an airport with a length of 5 km was floating at the sea surface within  $0.5 \text{ km} \leq x \leq 5.5 \text{ km}$ , and the still water depth  $h$  was uniform. An airplane ran on the floating airport in the positive direction of the  $x$ -axis. The grid size  $\Delta x$  was 20 m and the time interval  $\Delta t$  was 0.01 s.

We considered the movement of airplanes of two sizes—B747-400 and B737-800. The B747 series airplanes, nicknamed “jumbo jet”, continued growth in sales from the 1990s to the early 2000s, playing a leading role in long-haul international flights. In recent years, however, for reasons such as energy saving, more compact airplanes have become mainstream, including A320 and B737 jetliners, especially in the routes connecting domestic regional cities. Figure 6 shows the photographs of airplane models for size comparison.

For simplicity, we call the B747-400 and B737-800 airplanes B747 and B737, respectively, in this paper. The masses of B747 and B737 were set to 397,000 kgs and 79,000 kgs, respectively, referring to the maximum takeoff weights [36]. The unit “kgs” is often used for the mass of airplanes in aviation industry and is the same as “kg” in physics. In the 1D calculations, the tire contact distances of both B747 and B737 were assumed to be 9.8 m, considering the unit width of 1 m. In all 1D cases of touch-and-go, landing, and takeoff,

B747 ran from  $x = 1$  km to 4 km, whereas B737 ran from  $x = 1$  km to 3 km, on the floating airport. To simplify the conditions, we assumed that the point load due to the airplanes was constant while the airplanes were running on the airport, unlike in the following 2D calculations.



**Figure 6.** Photographs of the airplane models for size comparison. The upper model is B747-400 and the lower model is B737-800, which were produced by SkyMarks Models and Solaseed Air Inc., respectively. The length scale is 1/200.

### 3.1.2. Conditions for Touch-and-Go

In touch-and-go, an airplane lands on an airport, keeps running while preparing for takeoff, and takes off from the runway. This is part of basic training called “circuits and bumps”. In touch-and-go, both B747 and B737 were assumed to run at their constant speeds. The calculation conditions for touch-and-go are listed in Table 1. The values of flexural rigidity  $B$  were determined with reference to those obtained during the prototype test at the Mega-Float airport [37]. It should be noted that the airport length of 15 km is an unrealistic value set to ignore wave reflections at an edge of the airport.

**Table 1.** Calculation conditions for touch-and-go in the 1D calculations.

Case *	Airplane				Airport		Water Depth		
	Type (Mass)	Running Speed	Running Distance	Run Time	Length $L$	Flexural Rigidity $B$	$h$		
GA-L1	B747-400 (397,000 kgs)	83 m/s	3 km	36.1 s	15 km	$1 \times 10^{11}$ N·m	10 m		
GA-L2									10 m to 50 m
GA-S1					5 km			10 m, 20 m	
GA-S2								$1 \times 10^{10}$ N·m	10 m
GB-L1	B737-800 (79,000 kgs)	78 m/s	2 km	25.6 s	15 km		50 m		
GB-L2									10 m to 50 m
GB-S1					5 km				50 m

\* In the case names, GA and GB indicate the touch-and-go of B747 and B737, respectively, and L and S indicate that the airport is long and short, respectively.

### 3.1.3. Conditions for Landing

When an airplane lands on a floating airport, we assume that the airplane runs at a constant deceleration on the airport. In 1D problems, we consider the cases in which an airplane quickly shifts to taxiing when the running speed becomes sufficiently slow and leaves the runway, heading for a terminal. Therefore, after the run time, both the running speed and load of the airplane are assumed to be zero. The calculation conditions are listed in Table 2.

**Table 2.** Calculation conditions for landing in the 1D calculations.

Case *	Airplane					Airport		Water Depth
	Type (Mass)	Landing Speed **	Running Deceleration	Running Distance	Run Time	Length <i>L</i>	Flexural Rigidity <i>B</i>	<i>h</i>
LA-L	B747-400 (397,000 kgs)	72 m/s	0.86 m/s <sup>2</sup>	3 km	83.7 s	15 km	1 × 10 <sup>11</sup> N·m	10 m
LA-S						5 km		
LB-L	B737-800 (79,000 kgs)		1.3 m/s <sup>2</sup>	2 km	55.4 s	15 km	1 × 10 <sup>10</sup> N·m	50 m
LB-S						5 km		

\* In the case names, LA and LB indicate the landing of B747 and B737, respectively, and L and S after hyphen indicate that the airport is long and short, respectively. \*\* The landing speed is the airplane speed when the airplane touches down at the airport.

### 3.1.4. Conditions for Takeoff

When an airplane takes off from a floating airport, we assume that the airplane runs at a constant acceleration on the airport. In 1D problems, we consider the cases in which an airplane plays a rolling start—the airplane starts running to take off immediately after arriving at the starting point. Therefore, at the starting time, both the running speed and load of the airplane are assumed to be zero. The calculation conditions are listed in Table 3.

**Table 3.** Calculation conditions for takeoff in the 1D calculations.

Case *	Airplane					Airport		Water Depth
	Type (Mass)	Takeoff Speed **	Running Acceleration	Running Distance	Run Time	Length <i>L</i>	Flexural Rigidity <i>B</i>	<i>h</i>
TA-L	B747-400 (397,000 kgs)	83 m/s	1.15 m/s <sup>2</sup>	3 km	72.2 s	15 km	1 × 10 <sup>11</sup> N·m	10 m
TA-S						5 km		
TA-S-B								
TB-L	B737-800 (79,000 kgs)	78 m/s	1.52 m/s <sup>2</sup>	2 km	51.3 s	15 km	1 × 10 <sup>10</sup> N·m	
TB-S						5 km		

\* In the case names, TA and TB indicate the takeoff of B747 and B737, respectively, and L and S indicate that the airport is long and short, respectively. \*\* The takeoff speed is the airplane speed when the airplane leaves the airport.

## 3.2. 2D Calculations

### 3.2.1. Common Conditions

In 2D problems, we move a point load on a floating airport with a finite width. As sketched in Figure 7, the computational domain covers the area of  $0 \text{ km} \leq x \leq 6 \text{ km}$  and  $0 \text{ km} \leq y \leq 1 \text{ km}$ , and an airport is floating at the sea surface within  $0.5 \text{ km} \leq x \leq 5.5 \text{ km}$  and  $0 \text{ km} \leq y \leq 0.5 \text{ km}$ .

The perfect reflection condition was adopted along the *x*-axis, considering that the phenomena are axisymmetric with respect to the *x*-axis when an airplane runs along the *x*-axis. Therefore, the length and width of the airport were assumed to be 5 km and 1 km, respectively.

The still water depth *h* was uniformly 10 m, 20 m, or 100 m in the computational domain. The flexural rigidity of the airport, *B*, which was uniformly  $1.0 \times 10^{11} \text{ N}\cdot\text{m}^2$ , was given in the area covered by the airport, and it was possible to consider both the reflection and transmission of waves at the edges of the floating airport, including the side edges. The Sommerfeld open boundary condition was adopted at the lateral boundaries other than the *x*-axis. The grid sizes and time interval were  $\Delta x = \Delta y = 20 \text{ m}$  and  $\Delta t = 2.0 \times 10^{-4} \text{ s}$ , respectively.

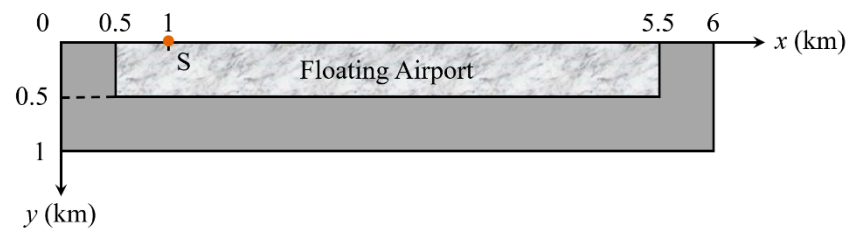


**Figure 7.** Computational domain for the 2D calculations. The floating airport is located in the marbled-colored area. The perfect reflection condition is adopted along the  $x$ -axis, so the  $x$ -axis is the neutral axis of the domain, assuming that the length and width of the airport are 5 km and 1 km, respectively. At Point S, located at  $x = 1$  km and  $y = 0$  km, an airplane touches down for landing and starts running for takeoff.

In the 2D problems, we selected a medium-sized passenger airplane, namely the B787-8 Dreamliner, which we simply call B787. B787 can be operated with approximately 20% less fuel than its predecessors, bringing the economy of large jetliners to the medium-sized airplane market. The mass of B787,  $M$ , was set to 228,400 kgs, referring to the maximum takeoff weight [36]. B787 touches down for landing and starts running for takeoff at Point S, located at  $x = 1$  km and  $y = 0$  km in Figure 7, and runs on the floating airport in the positive direction of the  $x$ -axis from Point S.

When normal stress  $\omega$  is applied to square grids in the horizontal plane, we assume that the distribution of the normal stress is a cone, the bottom of which is a circle of radius  $\Delta x$  centered at a grid point. Therefore, the normal stress  $\omega$  at the central grid point is applied, satisfying

$$M = \pi \Delta x^2 \omega / (3g). \tag{11}$$

### 3.2.2. Conditions for Landing

B787 lands on a floating airport in Case LC, in which the landing speed is 75 m/s. The deceleration is assumed to be constant during landing. To understand the phenomena more clearly, we take an example with a larger value of deceleration, namely  $3 \text{ m/s}^2$ , so that the running distance and run time are 0.938 km and 25 s, respectively. The conditions of Case LC are listed in Table 4.

**Table 4.** Calculation conditions in the 2D calculations.

Case *	Airplane					Airport		Water Depth
	Type (Mass)	Landing/Takeoff Speed **	Running Acceleration	Running Distance	Run Time	Length $L$	Flexural Rigidity $B$	$h$
LC	B787	75 m/s	$-3 \text{ m/s}^2$	0.938 km	25 s	5 km	$1 \times 10^{11} \text{ N}\cdot\text{m}^2$	10 m, 20 m,
TC	(228,400 kgs)		$3 \text{ m/s}^2$					or 100 m

\* In the case names, LC and TC indicate the landing and takeoff of B787, respectively. \*\* The landing and takeoff speeds are the airplane speeds when the airplane touches down at the airport and leaves the airport, respectively.

In the 2D calculations for landing, the load on the airport due to the airplane was zero at the touchdown time, i.e.,  $t = 0$  s, whereafter it increased linearly with time, and the full weight of the airplane was applied on the airport when the airplane stopped at  $t = 25$  s.

### 3.2.3. Conditions for Takeoff

B787 takes off from a floating airport in Case TC, in which the takeoff speed is 75 m/s. The acceleration is assumed to be constant during takeoff. For takeoff, we also consider a large value of acceleration, namely  $3 \text{ m/s}^2$ , so the running distance and run time are 0.938 km and 25 s, respectively, which are relatively short values. The conditions of Case TC are listed in Table 4.

In the 2D cases for takeoff, we assume that B787 has stopped and the field is in a steady state at  $t = 0$  s. Therefore, the full weight of the airplane is applied on the airport in a steady

state at  $t = 0$  s, and we numerically solve Equation (10) to obtain the initial displacement of the floating airport. After  $t = 0$  s, the airplane gradually accelerates and the load due to the airplane is assumed to decrease linearly with time, to become zero at the leaving time, i.e.,  $t = 25$  s, at which the airplane is completely away from the airport. After  $t = 25$  s, no loading onto the floating airport is carried out.

#### 4. 1D Response of a Floating Airport to Airplane Movement

##### 4.1. Touch-and-Go

We numerically simulated the motion of a floating airport when an airplane performs touch-and-go, by assuming that the airplane ran at a constant speed and the point load due to the airplane was constant while running. The calculation conditions are described in Table 1.

In Case GA-L1, B747 performed touch-and-go on a long-enough floating airport. The time variation of the floating airport and water surface profiles is depicted in Figure 8, in which the black dotted line indicates the location of the airplane running on the floating airport.

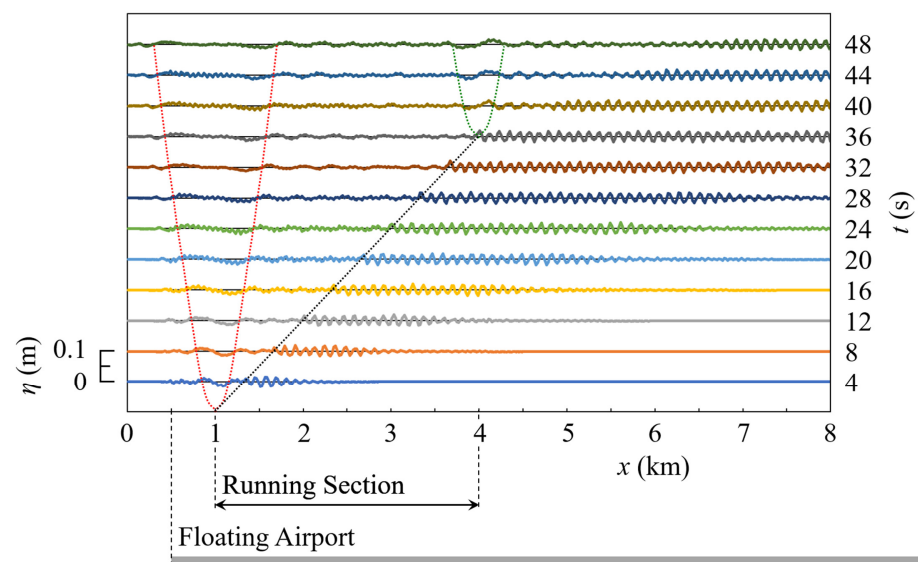


**Figure 8.** Profiles of the floating airport and water surface at every 4 s when B747 performed touch-and-go in Case GA-L1, the conditions of which are described in Table 1. The still water depth  $h$  was 10 m, the flexural rigidity of the airport,  $B$ , was  $1 \times 10^{11}$  N·m, and the airport length  $L$  was 15 km. The black dotted line indicates the location of the airplane running on the floating airport. The red and green dotted lines indicate the waves generated by the touchdown and leaving of the airplane, respectively.

When the airplane landed on the airport at  $t = 0$  s, the touchdown impact due to the airplane generated forward and backward waves, the propagation of which is indicated by the red dotted curves in Figure 8. While the airplane was running, a floating-body wave train with larger wave heights appeared in front of the airplane. However, the maximum wavelength of the floating-body waves produced by the running airplane was shorter than that generated by the touchdown impact. The generated floating-body waves traveled at velocities greater than the running velocity of the airplane. When the airplane took off at  $t = 36.1$  s, this leaving impact due to the airplane generated other waves, which are indicated by the green dotted curves in the figure. The maximum wavelength of these waves generated by the leaving impact was also longer than that of the waves due to the running airplane.

In Case GA-S1, the time variation of the floating airport and water surface profiles is depicted in Figure 9, in which the black dotted line indicates the location of the airplane running on the floating airport.

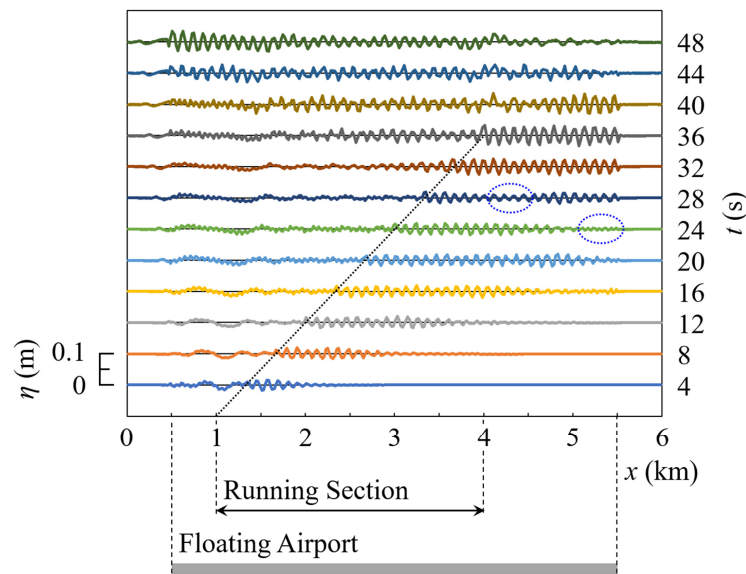


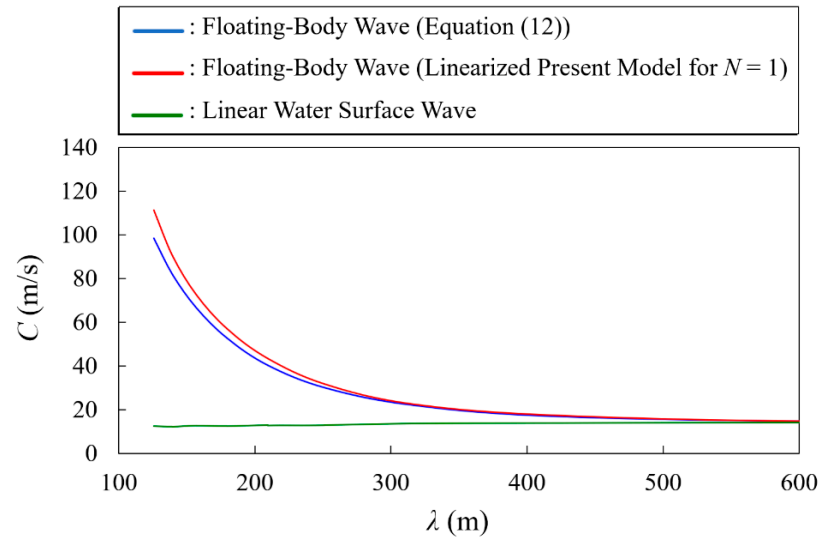
**Figure 9.** Profiles of the floating airport and water surface at every 4 s when B747 performed touch-and-go in Case GA-S1, the conditions of which are described in Table 1. The still water depth  $h$  was 10 m, the flexural rigidity of the airport,  $B$ , was  $1 \times 10^{11}$  N·m, and the airport length  $L$  was 5 km. The black dotted line indicates the location of the airplane running on the floating airport. The two blue dotted ellipses indicate examples of wave height reduction.

A floating-body wave generated by an airplane and reaching an end of a floating airport is divided into a reflected wave and a transmitted wave. The former is a floating-body wave that travels in the negative direction of the  $x$ -axis after being reflected at the airport edge, whereas the latter is a water wave that propagates in the positive direction of the  $x$ -axis. The wave height ratio between the former and the wave before reaching the airport edge is called reflectance in the present paper. Especially at  $t = 36$  s, large wave heights appeared based on the superposition of the waves reflected at the airport edge and the waves newly generated by the running airplane. There are two reasons why the reflectance of floating-body waves increases: (1) the wave energy attenuation is not effective, and (2) the difference between the traveling velocity of the floating-body waves and that of the water surface waves is large. Regarding the former, the wave energy attenuation was ignored in the present computation. A case study will be required because wave attenuation in a floating body depends on the type of structure and members. Conversely, to discuss the latter, we consider the dispersion relation of floating-body waves. When the draft of a floating thin plate is assumed to be zero, the linear dispersion relation of floating-body waves is expressed by

$$\theta^2 = \left( \frac{Bk^4}{m} + g \right) k \tanh(kh), \tag{12}$$

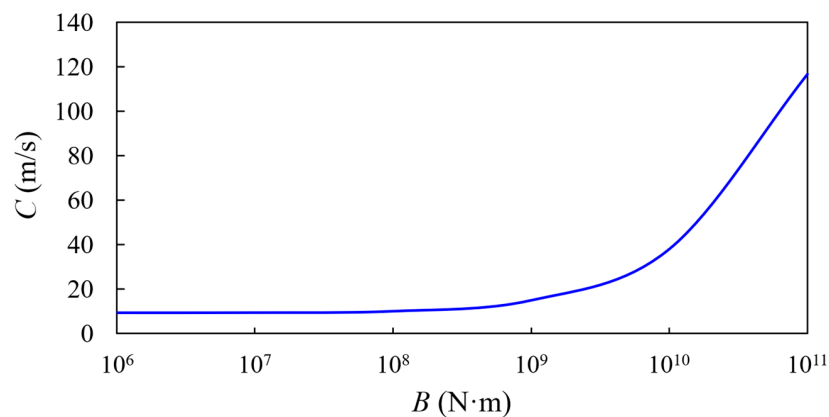
where  $\theta$  and  $k$  are the angular frequency and wavenumber of floating-body waves, respectively, and  $m$  is the density of the floating body [38]. As an example, Figure 10 displays the relationship between the traveling speed  $C$  and wavelength  $\lambda$  of floating-body waves evaluated by Equation (12) when  $B = 1.0 \times 10^{11}$  N·m,  $m = 1000$  kg/m<sup>3</sup>, and  $h = 20$  m. As depicted in Figure 10, we also obtained the corresponding numerical result of the linearized present model when the number of expansion terms for the velocity potential,  $N$ , is one, by considering the wave dispersion only due to the flexural rigidity of the floating body. For comparison, the phase velocity of linear water waves is depicted in the figure, which indicates that the difference in traveling velocity  $C$  between floating-body waves and water surface waves increases as the wavelength  $\lambda$  decreases. In Case GA-S1, the wavelength of the floating-body waves generated by the running airplane was less than 120 m based on

Figures 8 and 9. Moreover, the phase velocity of water waves decreases as the still water depth decreases in shallow water. Therefore, in Case GA-S1, the traveling velocity ratio between the floating-body waves and water waves was large, and the wave reflectance at the airport edges was large.



**Figure 10.** Traveling velocities of floating-body waves from Equation (12) and the linearized present model when the number of expansion terms for the velocity potential,  $N$ , is one. The flexural rigidity  $B$  and density  $m$  are  $1.0 \times 10^{11}$  N·m and  $1000$  kg/m<sup>3</sup>, respectively. The still water depth  $h$  is  $20$  m. The phase velocity of linear water waves is also depicted for comparison.

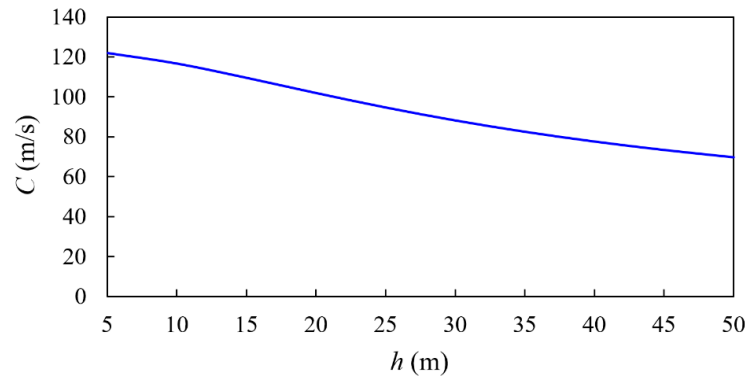
The relationships between the traveling velocity of floating-body waves,  $C$ , and the flexural rigidity of the floating body,  $B$ , is presented in Figure 11, using Equation (12), when the density of the floating body,  $m$ , is  $1000$  kg/m<sup>3</sup>, the wavelength of the floating-body waves is  $100$  m, and the still water depth  $h$  is  $10$  m. Based on the figure, as  $B$  is increased,  $C$  increases remarkably when  $B > 10^9$  N·m. When the flexural rigidity  $B$  decreases, the difference between the decreased traveling velocity of floating-body waves and the phase velocity of water waves decreases, so the wave reflectance is reduced. Thus, the reflectance of floating-body waves depends on both the flexural rigidity of an airport and the wavelength-to-water-depth ratio.



**Figure 11.** Relationship between the traveling velocity of floating-body waves,  $C$ , and the flexural rigidity of the floating body,  $B$ , using Equation (12). The density of the floating body,  $m$ , is  $1000$  kg/m<sup>3</sup>, the wavelength of the floating-body waves is  $100$  m, and the still water depth  $h$  is  $10$  m.

Moreover, the relationship between the traveling velocity of floating-body waves,  $C$ , and the still water depth  $h$  is depicted in Figure 12, using Equation (12), when  $B = 1.0 \times 10^{11}$  N·m,

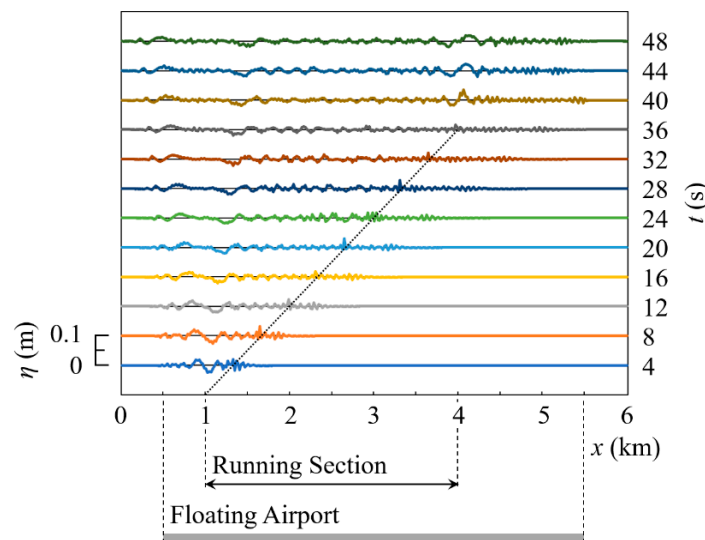
$m = 1000 \text{ kg/m}^3$ , and the wavelength of the floating-body waves is 100 m. Figure 12 indicates that  $C$  decreases as  $h$  is increased for the same wavelength.



**Figure 12.** Relationship between the traveling velocity of floating-body waves,  $C$ , and the still water depth  $h$ , using Equation (12). The flexural rigidity  $B$  and density  $m$  of the floating body are  $1.0 \times 10^{11} \text{ N}\cdot\text{m}$  and  $1000 \text{ kg/m}^3$ , respectively. The wavelength of the floating-body waves is 100 m.

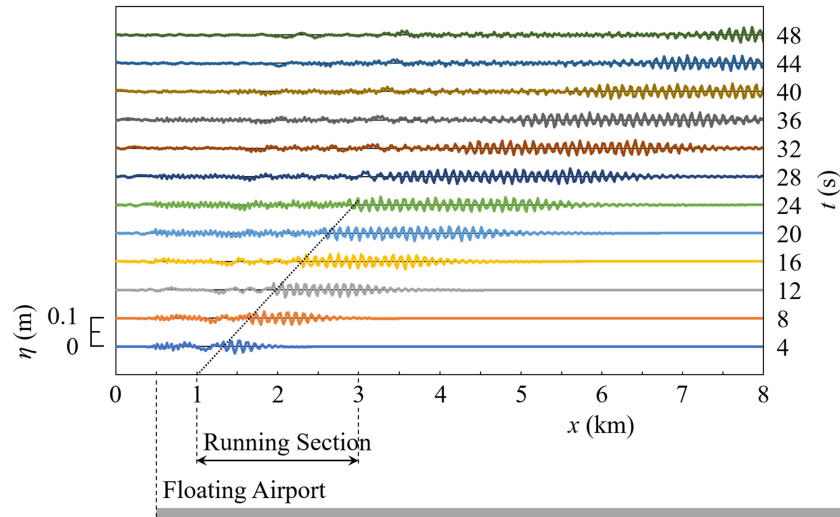
In Figure 9, at  $t = 48 \text{ s}$ , the reflected waves mentioned above, the re-reflected waves at another edge of the airport, and the waves produced by the touchdown impact due to the airplane are superposed. Conversely, within the two blue dotted ellipses depicted in the figure, the wave height is reduced because the phase of the waves newly produced by the running airplane and that of the reflected waves happen to be close to opposite. If the reflectance of floating-body waves at airport edges is large, it is necessary to pay attention to the long-lasting vibrations of the floating airport for flight landing and takeoff. A method of reducing the reflectance will be described in Section 4.3.

Figure 13 depicts the time variation of the floating airport and water surface profiles in Case GA-S2, which was obtained by reducing the flexural rigidity  $B$  from Case GA-S1. Comparing Figure 13 with Figure 9 for Case GA-S1, both the wavelength and traveling velocity of the floating-body waves generated by the running airplane decreased, so the total length of the floating-body wave train decreased.



**Figure 13.** Profiles of the floating airport and water surface at every 4 s when B747 performed touch-and-go in Case GA-S2, the conditions of which are described in Table 1. The still water depth  $h$  was 10 m, the flexural rigidity of the airport,  $B$ , was  $1 \times 10^{10} \text{ N}\cdot\text{m}$ , and the airport length  $L$  was 5 km. The black dotted line indicates the location of the airplane running on the floating airport.

Conversely, when B737 performed touch-and-go in Cases GB-L1 and GB-S1, the time variations of the floating airport and water surface profiles are depicted in Figures 14 and 15, respectively. Comparing these results, in Case GB-S1 with an airport of limited length, the wave heights of the floating-body waves were also larger near the edge of the airport because of wave superposition based on the high reflectance of the floating-body waves at the airport edge.



**Figure 14.** Profiles of the floating airport and water surface at every 4 s when B737 performed touch-and-go in Case GB-L1, the conditions of which are described in Table 1. The still water depth  $h$  was 50 m, the flexural rigidity of the airport,  $B$ , was  $1 \times 10^{10}$  N·m, and the airport length  $L$  was 15 km. The black dotted line indicates the location of the airplane running on the floating airport.

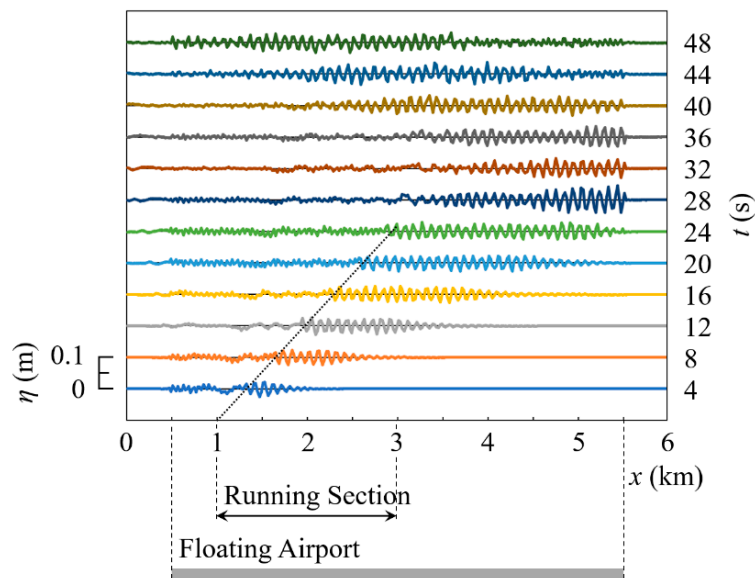


**Figure 15.** Profiles of the floating airport and water surface at every 4 s when B737 performed touch-and-go in Case GB-S1, the conditions of which are described in Table 1. The still water depth  $h$  was 50 m, the flexural rigidity of the airport,  $B$ , was  $1 \times 10^{10}$  N·m, and the airport length  $L$  was 5 km. The black dotted line indicates the location of the airplane running on the floating airport.

Comparing Figures 14 and 15 with Figures 8 and 9, B737 produced floating-body waves with wave heights comparable to those of B747 because the water depth was larger for the former than for the latter. When the still water depth is larger, i.e.,  $h = 20$  m, the time variation of the floating airport and water surface profiles in Case GA-S1 is depicted in

Figure 16. When the still water depth was increased, the wave heights of both the floating-body waves generated by the running airplane and those produced by the touchdown and leaving shocks due to the airplane increased in comparison with the results depicted in Figure 9 for  $h = 10$  m.

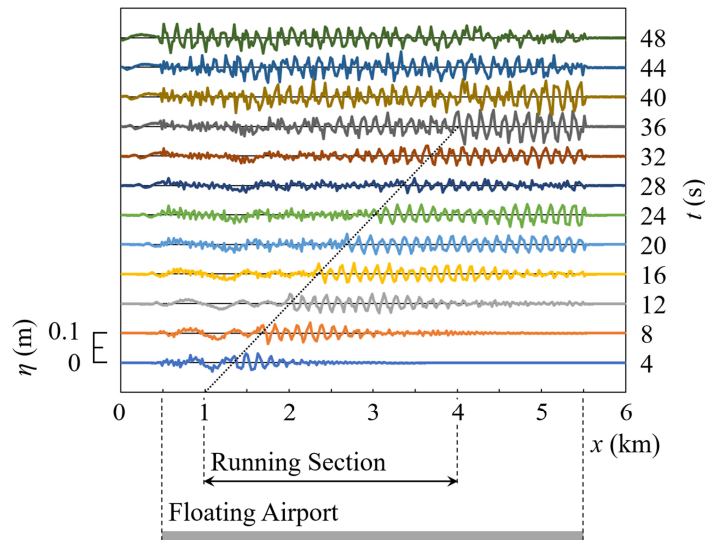


Figure 16. Profiles of the floating airport and water surface at every 4 s when B747 performed touch-and-go in Case GA-S1, the conditions of which are described in Table 1. The still water depth  $h$  was 20 m, the flexural rigidity of the airport,  $B$ , was  $1 \times 10^{11}$  N·m, and the airport length  $L$  was 5 km. The black dotted line indicates the location of the airplane running on the floating airport.

Figure 17 presents two examples of the relationships between the maximum displacement of the floating airport,  $\eta_{max}$ , and the still water depth  $h$  in Cases GA-L2 and GB-L2, when B747 and B737 left the long-enough airport in touch-and-go, respectively. These relationships are linearly approximated by  $\eta_{max} = 0.0025h + 0.013$  and  $\eta_{max} = 0.0009h + 0.0087$  (unit length in meter), respectively. When installing a floating airport in deeper water, it should be noted that the wave height of floating-body waves may increase because of airplane movement. The reason why larger water depths produce larger floating-body waves due to a running airplane will be discussed in Section 4.2.

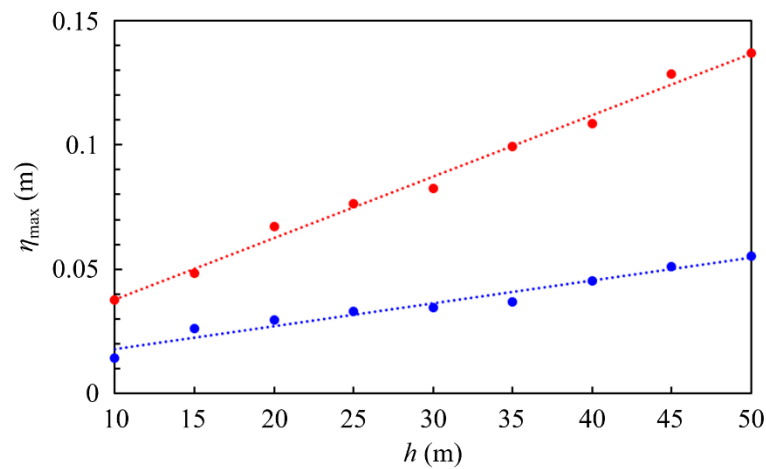
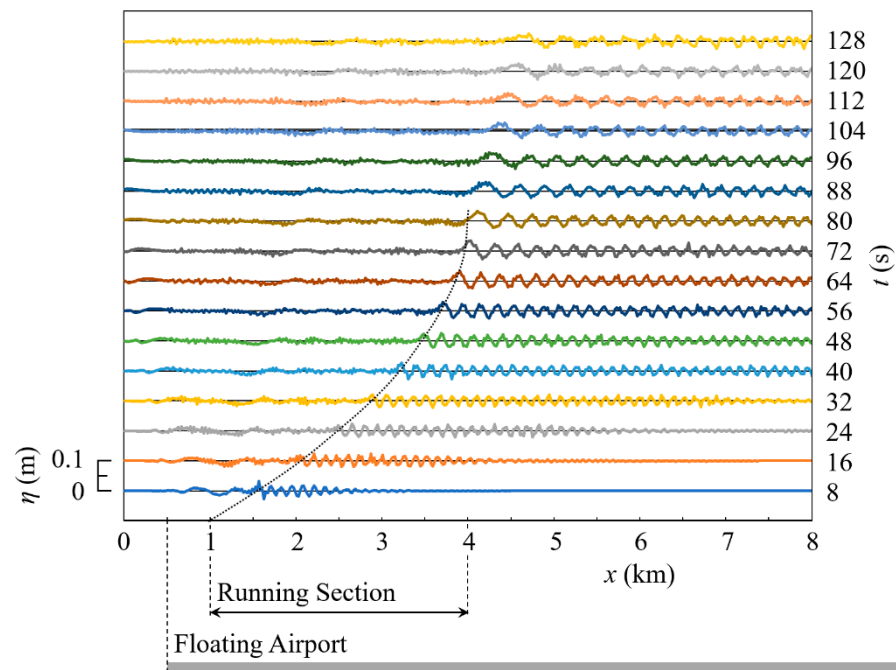


Figure 17. Relationships between the maximum displacement of the floating airport,  $\eta_{max}$ , and the still water depth  $h$  in Cases GA-L2 (red) and GB-L2 (blue), when B747 and B737 left the airport in touch-and-go, respectively. The conditions of these cases are described in Table 1. The flexural rigidity of the airport,  $B$ , was  $1 \times 10^{11}$  N·m in Case GA-L2, whereas  $B$  was  $1 \times 10^{10}$  N·m in Case GB-L2. The airport length  $L$  was 15 km in both cases.

### 4.2. Landing

We numerically simulated the motion of a floating airport when an airplane lands, by assuming that the airplane ran at a constant deceleration and the point load due to the airplane was constant while running. The calculation conditions are described in Table 2.

When B747 landed on a long-enough floating airport in Case LA-L, the time variation of the floating airport and water surface profiles is depicted in Figure 18. As the running speed of the airplane slowed down, both the wave height and wavelength of the floating-body waves generated by the running airplane increased. Based on the results of the one-dimensional propagation calculations [22], floating-body waves are significantly amplified when the moving speed of a point load on a floating thin plate is close to the phase velocity of the linear shallow-water waves, i.e.,  $\sqrt{gh}$ , in shallow-water conditions. This is due to resonance similar to that occurring in tsunami generation due to atmospheric-pressure waves, e.g., [39], based on the Proudman resonance [40]. Such resonance phenomena, often with a tail including waves of short wavelengths, are also known in other transient waves, e.g., [41–46]. In Case LA-L,  $\sqrt{gh}$  is approximately 9.9 m/s, which corresponds to the running speed of the airplane at  $t \approx 72$  s, near its stop time. Therefore, the airplane produced larger floating-body waves as it approached a stop. As depicted in Figure 17 for touch-and-go, the wave height of the floating-body waves increases as the still water depth increases, the reason for which is that the traveling speeds of the airplane and water waves become closer.



**Figure 18.** Profiles of the floating airport and water surface at every 8 s when B747 landed in Case LA-L, the conditions of which are described in Table 2. The still water depth  $h$  was 10 m, the flexural rigidity of the airport,  $B$ , was  $1 \times 10^{11}$  N·m, and the airport length  $L$  was 15 km. The black dotted line indicates the location of the airplane running on the floating airport.

In more detail, at landing, when the running speed of an airplane approaches the phase velocity of water waves, a “forced wave” is generated and amplified. In the present paper, a wave that follows the airplane is called a forced wave even if it contains a free-wave component in the resonance process. The generated forced waves do not satisfy the dispersion relation of floating-body waves, so the waves are disintegrated to produce “free waves” that satisfy the dispersion relation with traveling velocities larger than the airplane speed. The restraint by the airplane is released at the stop time of the airplane, whereafter the floating-body wave with the maximum wave height also propagates as a free wave.

Conversely, in Case GA-L1, in which B747 performed touch-and-go as described above, effective amplification did not occur because the airplane speed was too fast, and it was not close to the water wave speed at the water depth. While energy was being supplied by the running airplane, modest forced waves were generated and free waves continued to occur so as to satisfy the dispersion relation. Thus, large floating-body waves were not generated, not even by the jumbo jet.

Furthermore, although the landing impact due to the airplane at  $t = 0$  s generated floating-body waves, as in the above cases of touch-and-go, no shock wave appeared when the airplane came to a stop because the airplane slowed down gradually.

When B747 landed on a floating airport of limited length in Case LA-S, the time variation of the floating airport and water surface profiles is depicted in Figure 19. The figure indicates that the floating-body waves reflected at the airport edge were superposed with the waves newly created by the running airplane. However, after  $t = 72$  s, transmitted waves clearly appeared from the airport edge. Immediately after landing, the airplane speed was larger and the wavelength of the generated floating-body waves was shorter, so the wave reflectance was larger. Thereafter, as the airplane speed slowed down, the wavelength of the floating-body waves increased, and the wave reflectance decreased, as described above for Figure 10. Thus, some time after landing, transmitted waves may begin to appear.

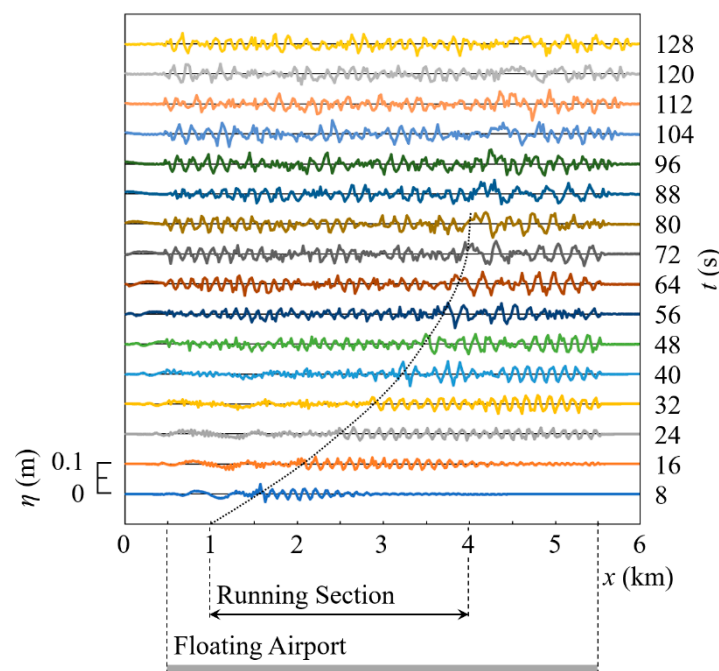


**Figure 19.** Profiles of the floating airport and water surface at every 8 s when B747 landed in Case LA-S, the conditions of which are described in Table 2. The still water depth  $h$  was 10 m, the flexural rigidity of the airport,  $B$ , was  $1 \times 10^{11}$  N·m, and the airport length  $L$  was 5 km. The black dotted line indicates the location of the airplane running on the floating airport.

When B737 landed on a long-enough floating airport in Case LB-L, the time variation of the floating airport and water surface profiles is depicted in Figure 20. Based on the figure, as the airplane speed decreased, the wave height of the generated floating-body waves increased, as in the cases of B747. It should be noted that the amplification factor of the wave height due to B737 in Figure 20 is larger than that due to B747 in Figure 18. As far as the flexural rigidity of the floating airport,  $B$ , is concerned, when  $B$  decreases, the traveling velocity of floating-body waves,  $C$ , decreases, as indicated in Figure 11. In the case of Figure 20,  $B$  decreased and  $C$  decreased, so the wavelength decreased, also depending on the relationship between  $C$  and the airplane speed. Moreover, the deceleration of B737 was

larger than that of B747; hence, the floating-body waves were generated more effectively by B737 running at a slower speed. Consequently, combined with the deeper water, the maximum wave height generated by B737 became larger than that due to B747.

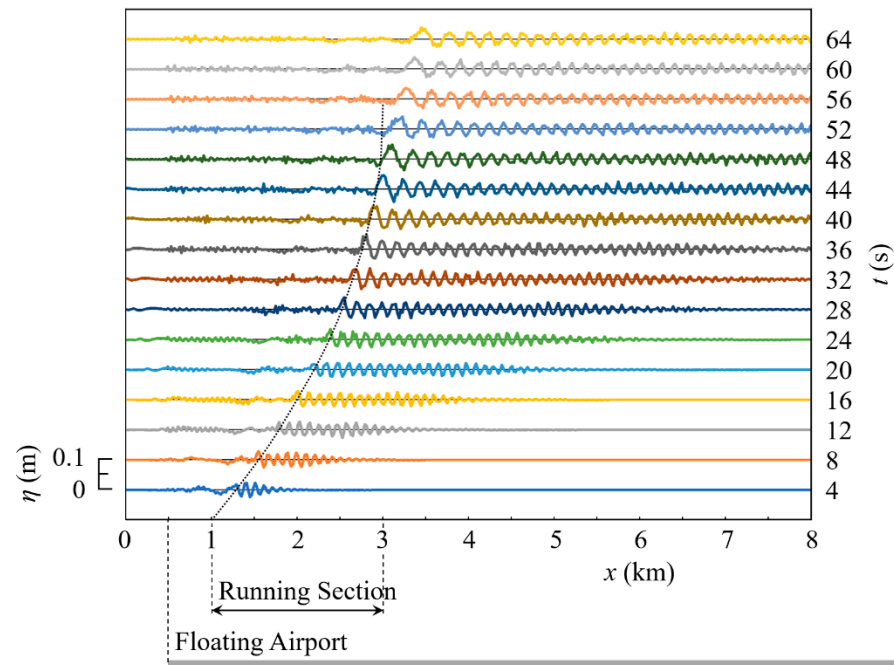


**Figure 20.** Profiles of the floating airport and water surface at every 4 s when B737 landed in Case LB-L, the conditions of which are described in Table 2. The still water depth  $h$  was 50 m, the flexural rigidity of the airport,  $B$ , was  $1 \times 10^{10}$  N·m, and the airport length  $L$  was 15 km. The black dotted line indicates the location of the airplane running on the floating airport.

Furthermore, when B737 landed on a floating airport of limited length in Case LB-S, the time variation of the floating airport and water surface profiles is depicted in Figure 21. Comparing this figure with Figure 19, because of the reduced flexural rigidity, the traveling velocity of the floating-body waves generated by the running airplane decreased, as described above, whereas the water wave speed increased in the deeper water. Thus, the transmitted waves from the airport edge started appearing at  $t = 52$  s, earlier than in the case for Figure 19.

In the present paper, the acceleration of the light airplane was increased using the values close to the current actual conditions. However, in less congested airports, reverse thrust can be reduced to save fuel, allowing airplanes to land over longer distances. Future studies will also consider the cases of the same traveling speed but different airplane types.

#### 4.3. Takeoff

We numerically simulated the motion of a floating airport when an airplane takes off, by assuming that the airplane ran at a constant acceleration and the point load due to the airplane was constant while running. The calculation conditions are described in Table 3.

When B747 took off from a long-enough floating airport in Case TA-L, the time variation of the floating airport and water surface profiles is depicted in Figure 22. Moreover, when B747 took off from a floating airport of limited length in Case TA-S, the result is depicted in Figure 23.

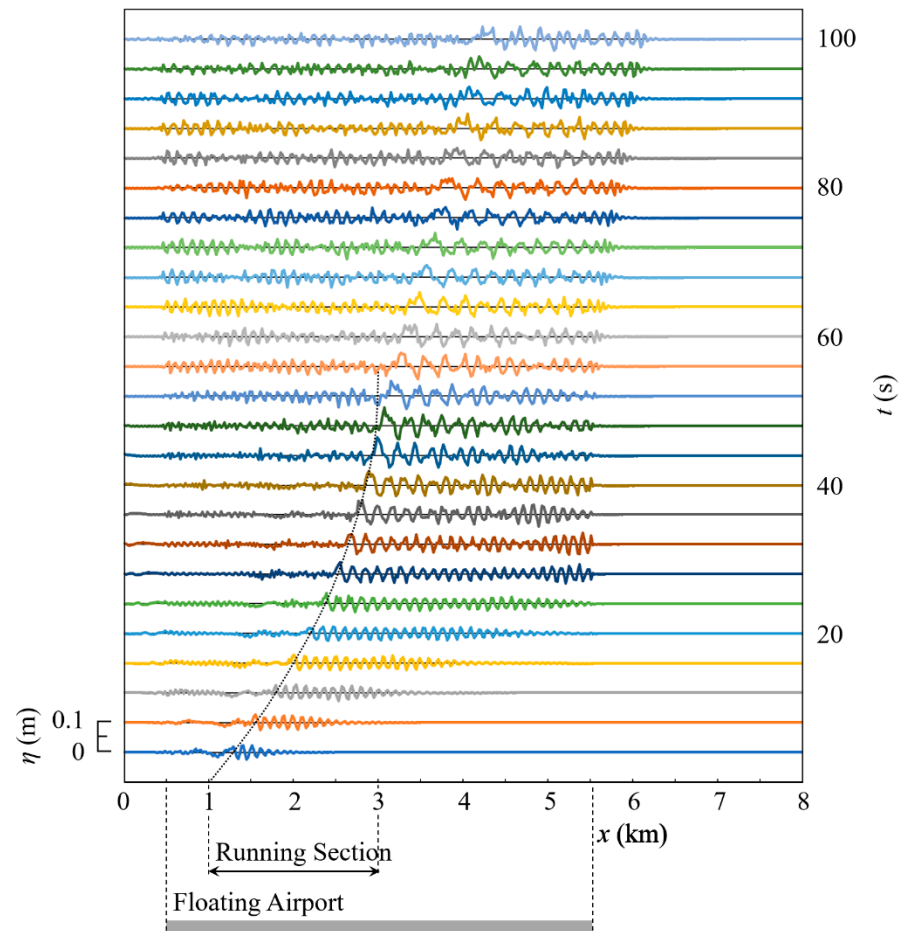


**Figure 21.** Profiles of the floating airport and water surface at every 4 s when B737 landed in Case LB-S, the conditions of which are described in Table 2. The still water depth  $h$  was 50 m, the flexural rigidity of the airport,  $B$ , was  $1 \times 10^{10}$  N·m, and the airport length  $L$  was 5 km. The black dotted line indicates the location of the airplane running on the floating airport.

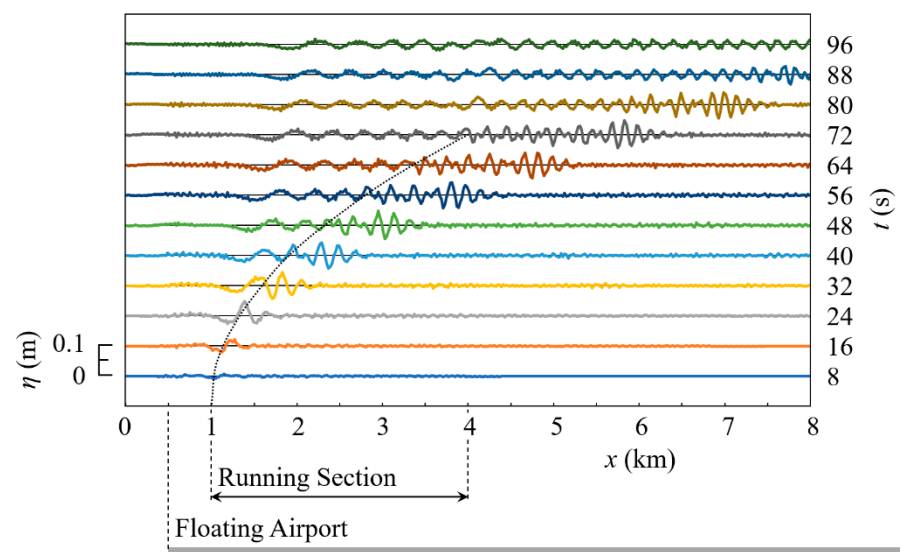


**Figure 22.** Profiles of the floating airport and water surface at every 8 s when B747 took off in Case TA-L, the conditions of which are described in Table 3. The still water depth  $h$  was 10 m, the flexural rigidity of the airport,  $B$ , was  $1 \times 10^{11}$  N·m, and the airport length  $L$  was 15 km. The black dotted line indicates the location of the airplane running on the floating airport.

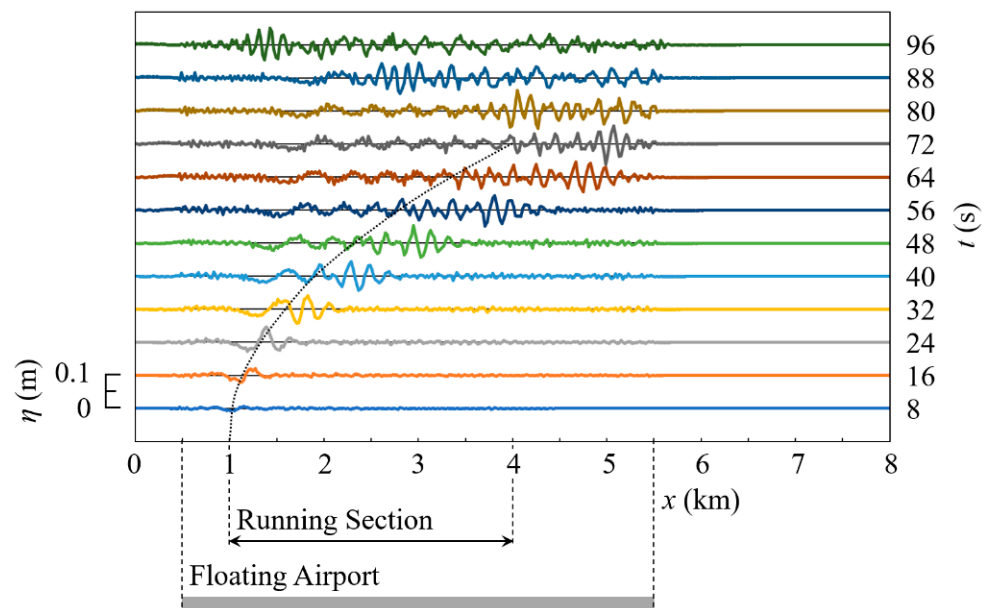


**Figure 23.** Profiles of the floating airport and water surface at every 8 s when B747 took off in Case TA-S, the conditions of which are described in Table 3. The still water depth  $h$  was 10 m, the flexural rigidity of the airport,  $B$ , was  $1 \times 10^{11}$  N·m, and the airport length  $L$  was 5 km. The black dotted line indicates the location of the airplane running on the floating airport.

Based on Figures 22 and 23, during the takeoff, much of the floating-body wave energy generated by the running airplane was localized in a short interval, resulting in a “wave clump” or wave group with a waveform like a discrete breather. The wavelength of the waves in the clump was approximately 170 m, and the traveling speed of the wave clump was approximately 43 m/s from Equation (12). The airplane reached this speed at  $t \approx 37$  s after departure. Although the traveling velocity of the wave clump did not reach 43 m/s for a while after its generation, the wave clump, which was produced by the slow-moving airplane shortly after its departure, traveled faster than the airplane. Thus, the wave clump traveling ahead of the airplane was followed by the waves newly generated by the running airplane.

To explain the above based on resonance, at takeoff, while airplane speed is close to water wave speed, the airplane generates and amplifies a forced wave based on the resonance. Thereafter, as the airplane speed increases and the difference in traveling speed between the airplane and the water waves increases, the restraint by the airplane is gradually released, and the amplified wave propagates as a free wave at a traveling velocity greater than the airplane speed. Therefore, the wave clump, which has been formed by changing the wave profile of the forced wave generated and amplified in a limited time, propagates in front of the airplane.

Conversely, when B737 took off from a long-enough floating airport and one of limited length in Cases TB-L and TB-S, respectively, the time variations of the floating airport and water surface profiles are depicted in Figures 24 and 25, respectively. Comparing these figures with Figures 22 and 23, when B737 takes off in deeper water, it may produce floating-body waves with a wave height similar to that of B747 in shallower water, depending on the flexural rigidity of the airport.

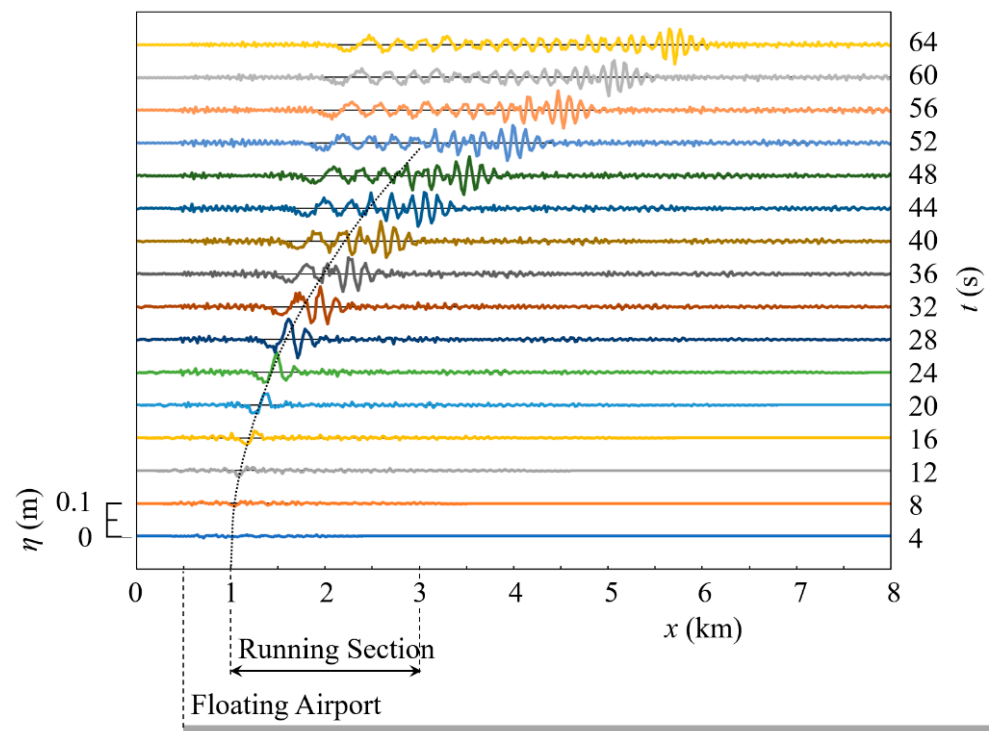


**Figure 24.** Profiles of the floating airport and water surface at every 4 s when B737 took off in Case TB-L, the conditions of which are described in Table 3. The still water depth  $h$  was 50 m, the flexural rigidity of the airport,  $B$ , was  $1 \times 10^{10}$  N·m, and the airport length  $L$  was 15 km. The black dotted line indicates the location of the airplane running on the floating airport.

To mitigate the hydroelastic vibration of a VLFS under wave action, several methods have been proposed: for example, the introduction of floating breakwaters [47], aircushions [48], and member connectors [49]. The reduction of the resonance phenomena due to the presence of a breakwater near a VLFS was also investigated [50]. If airplanes land or take off while floating airport vibration remains, unexpected large floating-body waves may occur because of wave superposition. As one of the methods of lowering the wave reflectance at the edges of a floating airport, we consider reducing the flexural rigidity of the airport,  $B$ , near the airport edges. In Case TA-S-B, the airplane to take off is B747 and the still water depth is 50 m. We numerically evaluated the wave reflectance  $R$  from the maximum wave heights before and after the first reflection at the airport edge. When  $B$  was  $1 \times 10^{11}$  N·m throughout the airport for  $0.5 \text{ km} \leq x \leq 5.5 \text{ km}$ ,  $R$  was approximately 0.67. Conversely, when  $B$  was  $1 \times 10^{11}$  N·m for  $0.5 \text{ km} \leq x < 5 \text{ km}$ , and  $1 \times 10^{10}$  N·m for  $5 \text{ km} \leq x \leq 5.5 \text{ km}$ ,  $R$  was approximately 0.55. This reduction in wave reflectance was due to two-stage reflection, which suppressed the wave height of the reflected waves. Furthermore, when  $B$  was  $1 \times 10^{11}$  N·m for  $0.5 \text{ km} \leq x < 5 \text{ km}$ , and  $B$  decreased linearly from  $1 \times 10^{11}$  N·m at  $x = 5 \text{ km}$  to  $1 \times 10^9$  N·m at  $x = 5.5 \text{ km}$ ,  $R$  was approximately 0.27 because of successive reflection near the airport edge. Consequently, the wave reflectance was reduced by lowering  $B$  near the airport edge. Even if the flexural rigidity is structurally or economically fixed for most of a floating airport, the wave reflectance can be reduced by modifying the structure or installing accessories to lower the flexural rigidity only near the airport edges, leading to an increase in the calmness of the floating airport.

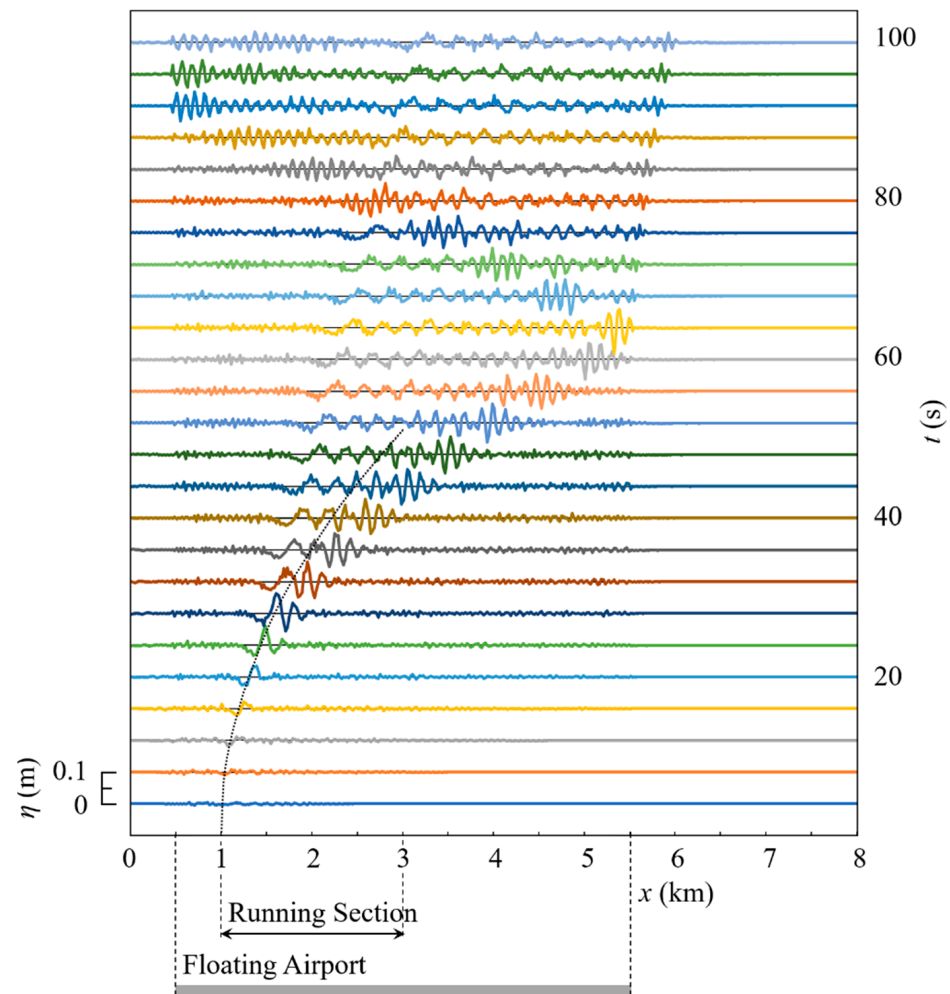


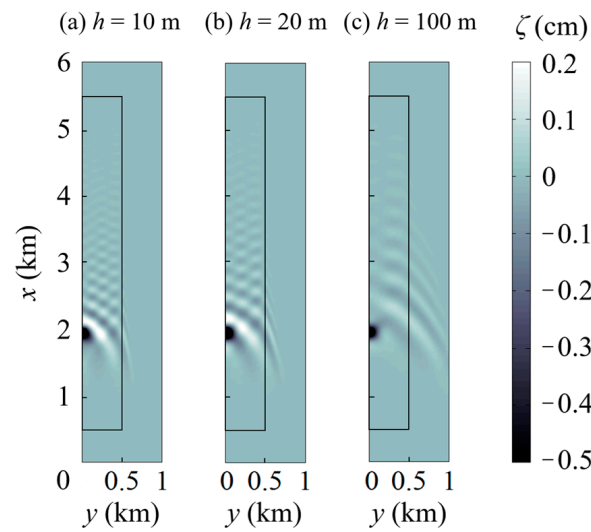
**Figure 25.** Profiles of the floating airport and water surface at every 4 s when B737 took off in Case TB-S, the conditions of which are described in Table 3. The still water depth  $h$  was 50 m, the flexural rigidity of the airport,  $B$ , was  $1 \times 10^{10}$  N·m, and the airport length  $L$  was 5 km. The black dotted line indicates the location of the airplane running on the floating airport.

## 5. 2D Response of a Floating Airport to Airplane Movement

### 5.1. Landing

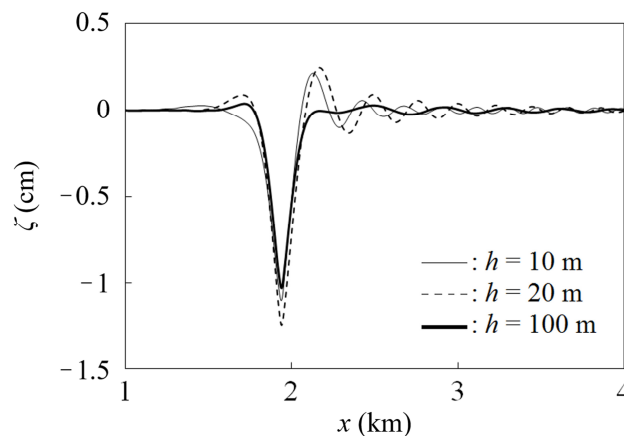
We numerically simulated the two-dimensional motion of a floating airport when B787 lands in Case LC, by assuming that the airplane ran at a constant deceleration and the point load due to the airplane increased linearly with time while running. The calculation conditions are described in Table 4.

Figure 26 presents the surface level distributions at  $t = 25$  s, at which B787 stopped after landing, for different still water depths  $h$ . As indicated in the figure, numerous surface waves exhibiting directional dispersion propagated and reflected at the airport edges. As a result, the superposition of the floating-body waves formed grid-like surface profiles at the airport. As the still water depth increases, the difference in propagation speed between the floating-body waves and water waves is reduced, so the wave reflectance at the airport edges decreases. Therefore, when  $h = 100$  m in Case LC, the grid-like pattern was suppressed at the floating airport compared to when the still water depth is shallower.



**Figure 26.** Surface-level distributions at  $t = 25$  s, at which B787 stopped after landing on the floating airport in Case LC. The still water depth  $h$  values were 10 m, 20 m, and 100 m for the figures on the left (a), middle (b), and right (c), respectively. The flexural rigidity of the airport,  $B$ , was  $1 \times 10^{11}$  N·m<sup>2</sup>.

Figure 27 depicts the surface profiles along the  $x$ -axis, which includes the longitudinal centerline of the floating airport, at the stop time  $t = 25$  s, for different still water depths in Case LC. The order of the results was the same as that of the existing horizontally two-dimensional results for a jumbo jet [27], although the maximum values of the present results were less because of the different airplane weights, decelerations, etc. When the still water depth  $h$  is 20 m, the phase velocity of linear shallow-water waves, i.e.,  $\sqrt{gh}$ , is 14 m/s, which corresponds to the airplane speed at  $t \approx 20$  s. At around this time, the point load due to the airplane was approximately 4/5ths of the maximum value and large enough to generate floating-body waves, resulting in a relatively large amplitude. Conversely, when  $h$  is 100 m,  $\sqrt{gh}$  is approximately 31.3 m/s, which corresponds to the airplane speed at  $t \approx 15$  s. At around this time, the point load was still only approximately 3/5ths of the maximum value, so the floating-body waves were not generated effectively.



**Figure 27.** Surface profiles along the  $x$ -axis at  $t = 25$  s, at which B787 stopped after landing in Case LC. The still water depth  $h$  values were 10 m, 20 m, and 100 m, and the flexural rigidity of the airport,  $B$ , was  $1 \times 10^{11}$  N·m<sup>2</sup>.

Figure 28a,b depict the time variations of the vertical positions of B787 and the surface gradients at the location of B787, respectively, for different still water depths in Case LC. As indicated in Figure 28a, the airplane position was gradually lowered. The surface-

gradient graphs are zigzag in Figure 28b because the values of the surface displacements are discretized at the grid points.

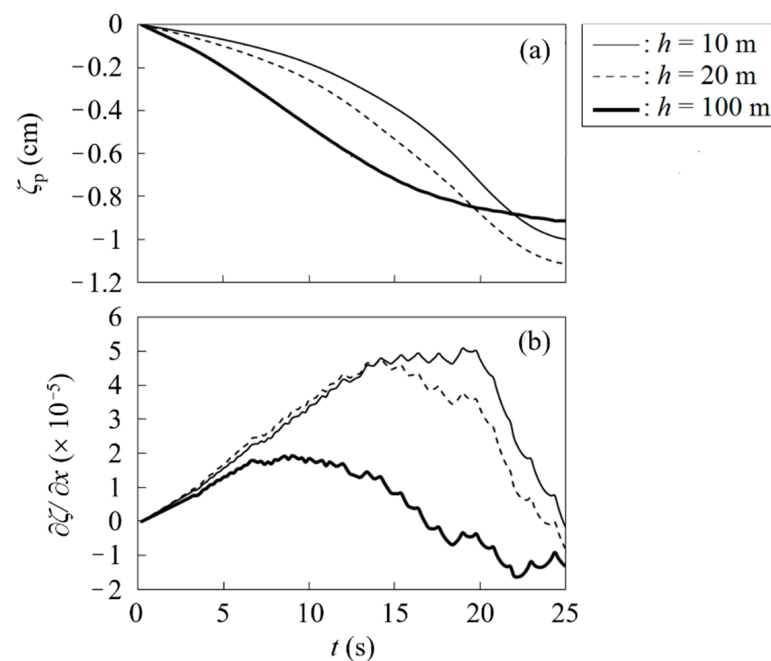


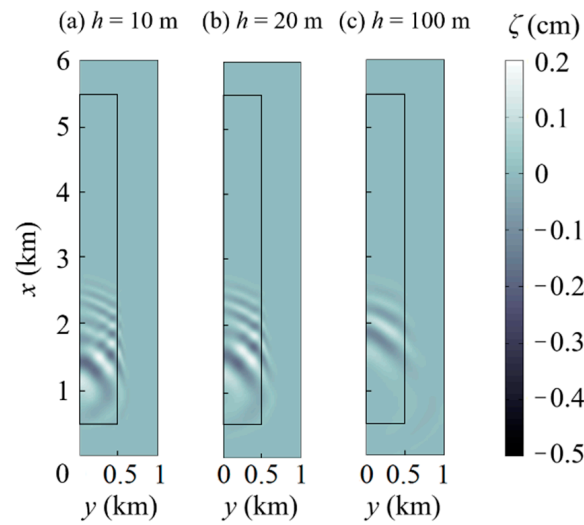
**Figure 28.** Time variations of the vertical positions of B787,  $\zeta_p$ , (a), and the surface gradient  $\partial\zeta/\partial x$  at the location of B787 (b), in Case LC, in which B787 stopped at  $t = 25$  s after landing. The still water depth  $h$  values were 10 m, 20 m, and 100 m, and the flexural rigidity of the airport,  $B$ , was  $1 \times 10^{11}$  N·m<sup>2</sup>.

During landing, the floating-body waves were generated by the airplane, as described above for the one-dimensional calculations, and Figure 28b indicates that the airport deflection caused the airplane to run uphill while the running speed of the airplane was large. The maximum upslope gradient of the floating airport beneath the airplane increased as the still water depth  $h$  decreased. When  $h = 10$  m, the airplane was on an upslope most of the time during landing. When  $h = 20$  m, the airplane ran downhill just before coming to a stop. Conversely, when  $h = 100$  m, the airplane was on a downslope for approximately 1/3rd of the landing time. It is necessary to pay attention to the gradient change of the runway in rolling an airplane.

### 5.2. Takeoff

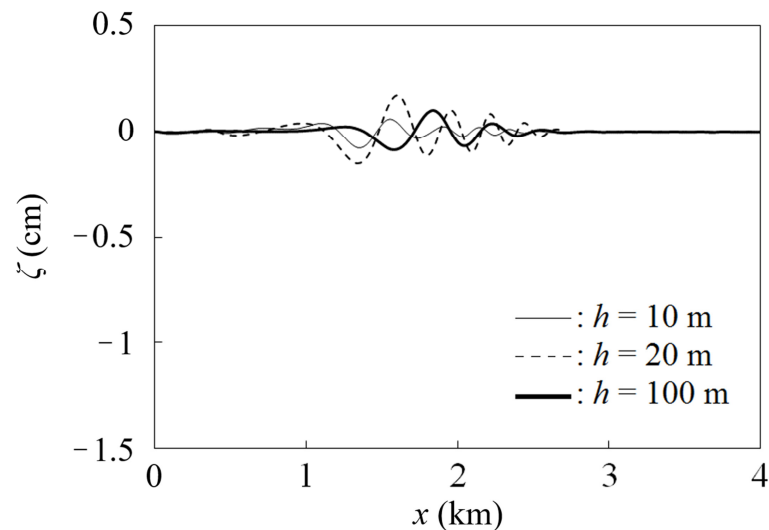
We numerically simulated the two-dimensional motion of a floating airport when B787 takes off in Case TC, by assuming that the airplane ran at a constant acceleration and the point load due to the airplane decreased linearly with time while running. The calculation conditions are described in Table 4.

Figure 29 depicts the surface-level distributions at  $t = 25$  s, at which B787 left the airport, for different still water depths  $h$ . Figure 29a,b indicate that grid-like patterns were also produced at the floating airport in takeoff when  $h = 10$  m and 20 m, respectively, although the grid-like patterns were not so remarkable as those in Figure 26a,b for landing. Conversely, when  $h = 100$  m, such a grid-like vibration was not formed at the floating airport. The grid-like oscillation did not appear in the existing results for relatively deep water, e.g., [27], and this phenomenon, which occurs based on the high wave reflectance at airport edges, is peculiar to floating airports with large flexural rigidity installed in shallower water.



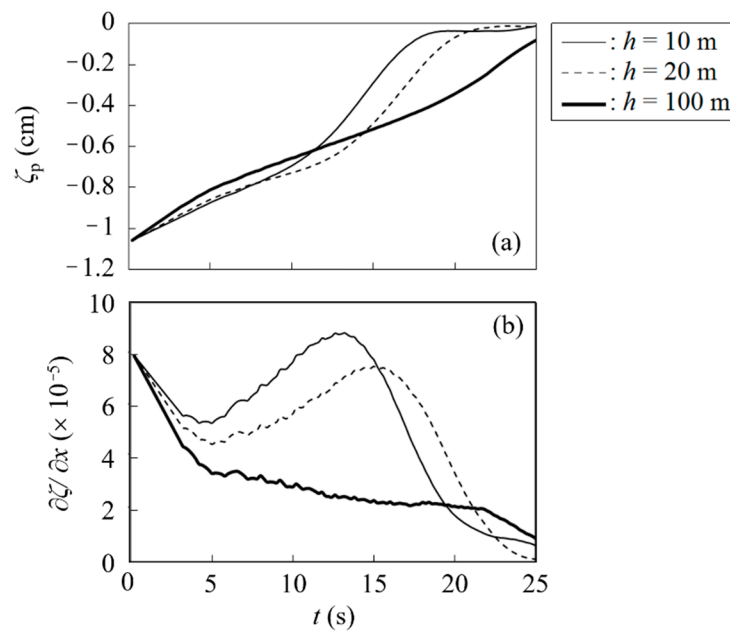
**Figure 29.** Surface-level distributions at  $t = 25$  s, at which B787 left the floating airport in Case TC. The still water depth  $h$  values were 10 m, 20 m, and 100 m for the figures on the left (a), middle (b), and right (c), respectively. The flexural rigidity of the airport,  $B$ , was  $1 \times 10^{11}$  N·m<sup>2</sup>.

Figure 30 depicts the surface profiles along the  $x$ -axis at  $t = 25$  s, at which B787 left the airport, for different still water depths in Case TC. When the still water depth  $h$  is 100 m, the phase velocity of linear shallow-water waves, i.e.,  $\sqrt{gh}$ , is approximately 31.3 m/s, which corresponds to the airplane speed at  $t \simeq 10$  s. Before this time, the point load due to the airplane was larger than 3/5ths of the maximum value. In addition, the wave clumps were produced when the running speed of the airplane was low, as indicated in Figures 22–25. Therefore, when  $h = 100$  m, larger floating-body waves were generated in takeoff than in landing.



**Figure 30.** Surface profiles along the  $x$ -axis at  $t = 25$  s, at which B787 left the airport in Case TC. The still water depth  $h$  values were 10 m, 20 m, and 100 m, and the flexural rigidity of the airport,  $B$ , was  $1 \times 10^{11}$  N·m<sup>2</sup>.

Moreover, Figure 31a,b present the time variations of the vertical positions of B787 and the surface gradients at the location of B787, respectively, for different still water depths in Case TC. As indicated in Figure 31a, although the airplane passed the peak of height when  $h = 10$  m and 20 m, the airplane position was increased most of the time during takeoff, which was different than during landing as depicted in Figure 28a.



**Figure 31.** Time variations of the vertical positions of B787,  $\zeta_p$ , (a), and the surface gradient  $\partial\zeta/\partial x$  at the location of B787 (b), in Case TC, in which B787 left the airport at  $t = 25$  s. The still water depth  $h$  values were 10 m, 20 m, and 100 m, and the flexural rigidity of the airport,  $B$ , was  $1 \times 10^{11}$  N·m<sup>2</sup>.

Figure 31b indicates that when taking off, the airplane ran on an upslope in a trough of the floating airport because we assumed that the floating airport was bending under the weight of the stationary airplane at  $t = 0$  s in Case TC. During takeoff, when  $h = 100$  m, the upslope gradient beneath the airplane decreased with time, whereas it dropped, then increased, and then dropped again when  $h = 10$  m and 20 m. For all these still water depths, the peak values of the upslope gradient were larger than those in landing depicted in Figure 28b. Therefore, during takeoff, the airplane ran on steeper slopes than during landing. For example, in Japan, the maximum longitudinal slope of a long airport runway is allowed up to 0.8% [51], and the calculated values of the slopes indicated in Figure 31b, as well as Figure 28b, are within the allowable range. However, if the floating-body waves from the previous landing/takeoff remain, or if the wave height of the reflected waves is large, the runway gradient may increase, not only in the traveling direction of the airplanes but also in the transverse direction. When the wave reflectance at the edges of a floating airport is large, it is necessary to take a sufficient time interval between landings and takeoffs.

### 6. Conclusions

Numerical simulations were generated to investigate the response of a very large floating airport to airplane movement using the set of nonlinear shallow water equations of velocity potential for water waves interacting with a floating thin plate.

First, the one-dimensional motion of a floating airport was simulated numerically when B747 and B737 performed touch-and-go, landing, and takeoff. During touch-and-go, when the running speed of the airplanes is much faster than the phase velocity of the water waves, effective amplification did not occur, and modest forced waves were generated while the airplanes were running, with many free waves ahead that satisfied the dispersion relation. However, when the airplane speed is closer to the water wave speed, even B737 produced large floating-body waves based on the resonance. Moreover, the impacts due to both the touchdown and leaving of the airplanes generated other forward and backward waves.

Conversely, during landing, when the airplane speed approached the water wave speed, a forced wave was generated and amplified based on the resonance. When the

airplanes stopped, the restraint from the airplanes was released, whereafter the amplified floating-body wave with the maximum wave height also propagated as a free wave.

During takeoff, while the airplane speed was close to the water wave speed, the airplanes also generated and amplified a forced wave. Thereafter, as the running speed of the airplanes increased and the difference in traveling speed between the airplanes and the water waves increased, the restraint from the airplanes was gradually released and the amplified wave propagated as a free wave at a traveling velocity greater than those of the airplanes. Therefore, the wave clump, which was formed by changing the wave profile of the forced wave generated and amplified shortly after starting to run, propagated in front of the airplanes.

If the reflectance of floating-body waves at airport edges is high, prolonged vibrations may interfere with the operation of airplanes and cause structural fatigue. When we tried lowering the flexural rigidity of the airport near its edge, the wave reflectance was reduced. In the present study, we ignored the attenuation of wave energy in the floating airport, so future work is required to consider wave energy attenuation by modifying the present model.

Second, the horizontally two-dimensional motion of a floating airport was simulated numerically when B787 performed landing and takeoff. When the still water depth is shallower, a grid-like pattern was formed on the floating airport. This pattern was due to the reflection of the floating-body waves with directional dispersion at the edges of the floating airport and appeared more remarkably in landing than in takeoff. In the 2D calculations, we assumed that the load of the airplane changed while running, so the effective amplification of waves occurred from the sufficient load applied when the airplane speed approached the water wave speed. Furthermore, the maximum upslope gradient beneath the airplane increased as the still water depth decreased, and it was larger in takeoff than in landing.

Although we used the numerical scheme for the water wave equations considering both wave nonlinearity and dispersion, we ignored the dispersion of water waves in the present study. In the future, we should simulate floating-body waves with more expansion terms of velocity potential when the frequency dispersion is significant, especially for an airport installed in deep water. It is also necessary to consider whether the plate equation can be linear since there may be cases where the nonlinearity of floating-body motion that does not interfere with airplane operation cannot be ignored.

**Author Contributions:** Conceptualization, T.K.; Methodology, T.K.; Validation, M.H.; Investigation, T.K.; Writing—original draft, T.K. All authors have read and agreed to the published version of the manuscript.

**Funding:** This work was supported by JSPS KAKENHI Grant Number JP22H01136, the Collaborative Research Program of Research Institute for Applied Mechanics, Kyushu University, and the Research Institute for Mathematical Sciences, an International Joint Usage/Research Center located in Kyoto University.

**Acknowledgments:** Sincere gratitude is extended to Nakayama, K., Kobe University, who built the original program code for internal wave calculations. The authors thank Yamashita, K., the Nuclear Regulation Authority, for his contribution to the 2D calculations when he was a member of our laboratory. The authors would like to express our thanks to the anonymous reviewers for their valuable comments that improved the article.

**Conflicts of Interest:** The authors declare no conflict of interest.

## References

1. Renzi, E.; Michele, S.; Zheng, S.; Jin, S.; Greaves, D. Niche applications and flexible devices for wave energy conversion: A review. *Energies* **2021**, *14*, 6537. [[CrossRef](#)]
2. Michele, S.; Zheng, S.; Greaves, D. Wave energy extraction from a floating flexible circular plate. *Ocean Eng.* **2022**, *245*, 110275. [[CrossRef](#)]

3. Kashiwagi, M. Research on hydroelastic responses of VLFS: Recent progress and future work. *Int. J. Offshore Polar Eng.* **2000**, *10*, 81–90.
4. Watanabe, E.; Utsunomiya, T.; Wang, C.M. Hydroelastic analysis of pontoon-type VLFS: A literature survey. *Eng. Struct.* **2004**, *26*, 245–256. [[CrossRef](#)]
5. Montiel, F.; Bonnefoy, F.; Ferrant, P.; Bennetts, L.; Squire, V.; Marsault, P. Hydroelastic response of floating elastic discs to regular waves. Part 1. Wave basin experiments. *J. Fluid Mech.* **2013**, *723*, 604–628. [[CrossRef](#)]
6. Zhang, X.; Lu, D.; Gao, Y.; Chen, L. A time domain discrete-module-beam-bending-based hydroelasticity method for the transient response of very large floating structures under unsteady external loads. *Ocean Eng.* **2018**, *164*, 332–349. [[CrossRef](#)]
7. Ding, J.; Wu, Y.; Xie, Z.; Yang, W.; Wang, S.; Yu, J.; Yu, T. Overview: Research on hydroelastic responses of VLFS in complex environments. *Mar. Struct.* **2021**, *78*, 102978. [[CrossRef](#)]
8. Michele, S.; Zheng, S.; Burianni, F.; Borthwick, A.G.L.; Greaves, D.M. Floating hydroelastic circular plate in regular and irregular waves. *Eur. J. Mech. B Fluids* **2023**, *99*, 148–162. [[CrossRef](#)]
9. Li, W.; Ke, S.; Chen, J.; Zhu, T.; Ren, H. Hydrodynamic response and energy analysis in a very large floating structure supporting a marine airport under typhoon-driven waves. *Ocean Eng.* **2022**, *266*, 112987. [[CrossRef](#)]
10. Squire, V.A.; Dugan, J.P.; Wadhams, P.; Rottier, P.J.; Liu, A.K. Of ocean waves and sea ice. *Annu. Rev. Fluid Mech.* **1995**, *27*, 115–168. [[CrossRef](#)]
11. Meylan, M.H.; Squire, V.A. Response of a circular ice floe to ocean waves. *J. Geophys. Res. Oceans* **1996**, *101*, 8869–8884. [[CrossRef](#)]
12. Sakai, S.; Hanai, K. Empirical formula of dispersion relation of waves in sea ice. In Proceedings of the Ice in the Environment: Proceedings of the 16th IAHR International Symposium on Ice, Dunedin, New Zealand, 2–6 December 2002; pp. 327–335. Available online: <https://www.iahr.org/library/infor?pid=19937> (accessed on 10 February 2023).
13. Meylan, M.H.; Bennetts, L.; Cavaliere, C.; Alberello, A.; Toffoli, A. Experimental and theoretical models of wave-induced flexure of a sea ice floe. *Phys. Fluids* **2015**, *27*, 041704. [[CrossRef](#)]
14. Waseda, T.; Alberello, A.; Nose, T.; Toyota, T.; Kodaira, T.; Fujiwara, Y. Observation of anomalous spectral downshifting of waves in the Okhotsk Sea Marginal Ice Zone. *Philos. Trans. R. Soc. A Math. Phys. Eng. Sci.* **2022**, *380*, 256. [[CrossRef](#)] [[PubMed](#)]
15. Părău, E.; Dias, F. Nonlinear effects in the response of a floating ice plate to a moving load. *J. Fluid Mech.* **2002**, *460*, 281–305. [[CrossRef](#)]
16. Dinvyay, E.; Kalisch, H.; Părău, E.I. Fully dispersive models for moving loads on ice sheets. *J. Fluid Mech.* **2019**, *876*, 122–149. [[CrossRef](#)]
17. Tugulan, C.; Trichtchenko, O.T.; Părău, E. Three-dimensional waves under ice computed with novel preconditioning methods. *J. Comput. Phys.* **2022**, *459*, 111129. [[CrossRef](#)]
18. Takagi, K. Interaction between solitary wave and floating elastic plate. *J. Waterw. Port Coastal Ocean Eng.* **1997**, *123*, 57–62. [[CrossRef](#)]
19. Sakai, S.; Liu, X.; Sasamoto, M.; Kagesa, T. Experimental and numerical study on the hydroelastic behavior of VLFS under tsunami. In *Hydroelasticity in Marine Technology*; Kashiwagi, M., Koterayama, W., Ohkusu, M., Eds.; Yomei Printing Cooperative Society: Fukuoka, Japan, 1998; pp. 385–392. ISBN 4-87780-001-8.
20. Kakinuma, T.; Ochi, N. Tsunami-height reduction using a very large floating structure. In *Mathematical Analysis of Continuum Mechanics and Industrial Applications III, CoMFOs 2018, Mathematics for Industry 34*; Ito, H., Hirano, S., Kimura, M., Kovtunen, V.A., Khludnev, A.M., Eds.; Springer: Singapore, 2020; pp. 193–202. [[CrossRef](#)]
21. Xu, F.; Lu, D.Q. Wave scattering by a thin elastic plate floating on a two-layer fluid. *Int. J. Eng. Sci.* **2010**, *48*, 809–819. [[CrossRef](#)]
22. Kakinuma, T.; Yamashita, K.; Nakayama, K. Surface and internal waves due to a moving load on a very large floating structure. *J. Appl. Math.* **2012**, *2012*, 830530. [[CrossRef](#)]
23. Kim, J.W.; Webster, W.C. The drag on an airplane taking off from a floating runway. *J. Mar. Sci. Technol.* **1998**, *3*, 76–81. [[CrossRef](#)]
24. Watanabe, E.; Utsunomiya, T.; Tanigaki, S. A transient response analysis of a very large floating structure by finite element method. *Struct. Eng./Earthq. Eng. JSCE* **1998**, *15*, 155s–163s. [[CrossRef](#)]
25. Hermans, A.J. A boundary element method for the interaction of free-surface waves with a very large floating flexible platform. *J. Fluids Struct.* **2000**, *14*, 943–956. [[CrossRef](#)]
26. Endo, H. The behavior of a VLFS and an airplane during takeoff/landing run in wave condition. *Mar. Struct.* **2000**, *13*, 477–491. [[CrossRef](#)]
27. Kashiwagi, M. Transient responses of a VLFS during landing and take-off of an airplane. *J. Mar. Sci. Technol.* **2004**, *9*, 14–23. [[CrossRef](#)]
28. Nguyen, X.V.; Luong, V.H.; Cao, T.N.T.; Lieu, X.Q.; Nguyen, T.B. Hydroelastic responses of floating composite plates under moving loads using a hybrid moving element-boundary element method. *Adv. Struct. Eng.* **2020**, *23*, 2759–2775. [[CrossRef](#)]
29. Kakinuma, T. Nonlinear interaction of surface and internal waves with very large floating or submerged structures. In *Fluid Structure Interaction II*; Chakrabarti, S.K., Brebbia, C.A., Almorza, D., Gonzalez-Palma, R., Eds.; WIT Press: Billerica MA, USA, 2003; pp. 117–126.
30. Luke, J.C. A variational principle for a fluid with a free surface. *J. Fluid Mech.* **1967**, *27*, 395–397. [[CrossRef](#)]
31. Isobe, M. Time-dependent mild-slope equations for random waves. In *Coastal Engineering 1994*; Edge, B.L., Ed.; ASCE: Reston, VA, USA, 1995; pp. 285–299. [[CrossRef](#)]

32. Iguchi, T. A Mathematical justification of the Isobe–Kakinuma model for water waves with and without bottom topography. *J. Math. Fluid Mech.* **2018**, *20*, 1985–2018. [[CrossRef](#)]
33. Matsuno, Y. Hamiltonian formulation of the extended Green–Naghdi equations. *Phys. D Nonlinear Phenom.* **2015**, *301–302*, 1–7. [[CrossRef](#)]
34. Nakayama, K.; Kakinuma, T. Internal waves in a two-layer system using fully nonlinear internal-wave equations. *Int. J. Numer. Methods Fluids* **2010**, *62*, 574–590. [[CrossRef](#)]
35. Kakinuma, T. A numerical study on distant tsunami propagation considering the strong nonlinearity and strong dispersion of waves, or the plate elasticity and mantle fluidity of Earth. *Fluids* **2022**, *7*, 150. [[CrossRef](#)]
36. Boeing Japan Homepage. Available online: <https://www.boeing.jp> (accessed on 10 February 2023).
37. Andrianov, A.O.I. Hydroelastic Analysis of Very Large Floating Structures. Ph.D. Thesis, Electrical Engineering, Mathematics and Computer Science, TU Delft, Delft, The Netherlands, 2005. Available online: <http://resolver.tudelft.nl/uuid:85cef785-c17c-41d7-9a58-6a183c468523> (accessed on 11 April 2023).
38. Tsubogo, T. A basic investigation on deflection wave propagation and strength of very large floating structures (the 2nd report). *J. Soc. Nav. Arch. Jpn.* **1997**, *1997*, 381–390. [[CrossRef](#)]
39. Kakinuma, T. Tsunamis generated and amplified by atmospheric pressure waves due to an eruption over seabed topography. *Geosciences* **2022**, *12*, 232. [[CrossRef](#)]
40. Proudman, J. The effects on the sea of changes in atmospheric pressure. *Geophys. J. Int.* **1929**, *2*, 197–209. [[CrossRef](#)]
41. Whitham, G.B. *Linear and Nonlinear Waves*; John Wiley & Sons, Inc.: New York, NY, USA, 1974; pp. 511–532. [[CrossRef](#)]
42. Wu, T. Generation of upstream advancing solitons by moving disturbances. *J. Fluid Mech.* **1987**, *184*, 75–99. [[CrossRef](#)]
43. Lee, S.; Yates, G.; Wu, T. Experiments and analyses of upstream-advancing solitary waves generated by moving disturbances. *J. Fluid Mech.* **1989**, *199*, 569–593. [[CrossRef](#)]
44. Kakinuma, T.; Akiyama, M. Numerical analysis of tsunami generation due to seabed deformation. In *Coastal Engineering 2006*; Smith, J.M., Ed.; World Scientific Publishing Co., Pte. Ltd.: Singapore, 2007; pp. 1490–1502. [[CrossRef](#)]
45. Dalphin, J.; Barros, R. Optimal shape of an underwater moving bottom generating surface waves ruled by a forced Korteweg-de Vries equation. *J. Optim. Theory Appl.* **2018**, *180*, 574–607. [[CrossRef](#)]
46. Michele, S.; Renzi, E.; Borthwick, A.; Whittaker, C.; Raby, A. Weakly nonlinear theory for dispersive waves generated by moving seabed deformation. *J. Fluid Mech.* **2022**, *937*, 94. [[CrossRef](#)]
47. Hong, D.C.; Hong, S.Y.; Hong, S.W. Reduction of hydroelastic responses of a very-long floating structure by a floating oscillating-water-column breakwater system. *Ocean Eng.* **2006**, *33*, 610–634. [[CrossRef](#)]
48. van Kessel, J.L.F.; Pinkster, J.A. The effect of aircushion division on the motions of large floating structures. In Proceedings of the ASME 2007 26th International Conference on Offshore Mechanics and Arctic Engineering, San Diego, CA, USA, 10–15 June 2007; pp. 677–686. [[CrossRef](#)]
49. Gao, R.P.; Wang, C.M.; Koh, C.G. Reducing hydroelastic response of pontoon-type very large floating structures using flexible connector and gill cells. *Eng. Struct.* **2013**, *52*, 372–383. [[CrossRef](#)]
50. Ohmatsu, S. Numerical calculation method for the hydroelastic response of a pontoon-type very large floating structure close to a breakwater. *J. Mar. Sci. Technol.* **2000**, *5*, 147–160. [[CrossRef](#)]
51. Regulation for Enforcement of the Civil Aeronautics Act. *Order Minist. Land Infrastruct. Transp. Tour.* **2008**, *73*, 79. Available online: <https://www.japaneselawtranslation.go.jp/en/laws/view/4052> (accessed on 10 February 2023).

**Disclaimer/Publisher’s Note:** The statements, opinions and data contained in all publications are solely those of the individual author(s) and contributor(s) and not of MDPI and/or the editor(s). MDPI and/or the editor(s) disclaim responsibility for any injury to people or property resulting from any ideas, methods, instructions or products referred to in the content.